1   **Title:** Defining the Syrian hamster as a highly susceptible preclinical model for SARS-CoV-2

2   infection

3

4   **Authors:** Kyle Rosenke[1], Kimberly Meade-White[1], Michael Letko[1#], Chad Clancy[2], Frederick

5   Hansen[1], Yanan Liu[3], Atsushi Okumura[1], Tsing-Lee Tang-Huau[1], Rong Li[3], Greg Saturday[2],

6   Friederike Feldmann[2], Dana Scott[2], Zhongde Wang[3], Vincent Munster[1], Michael A. Jarvis[1,4],

7   Heinz Feldmann[1]*

8

9   **Affiliation:** [1]Laboratory of Virology and [2]Rocky Mountain Veterinary Branch, Division of

10   Intramural Research, National Institute of Allergy and Infectious Diseases, National Institutes of

11   Health, Hamilton, MT, USA; [3]Department of Animal, Dairy, and Veterinary Sciences, Utah

12   State University, Logan, UT, USA; [4]University of Plymouth and The Vaccine Group Ltd,

13   Plymouth, Devon, UK

14

15   **#Current affiliation:** Paul G. Allen School for Global Animal Health, Washington State

16   University, Pullman, WA, USA.

17

18   ***Corresponding author:** Heinz Feldmann, Rocky Mountain Laboratories, 903 S 4th Street,

19   Hamilton, MT, US-59840; Tel: (406)-375-7410; Email: feldmannh@niaid.nih.gov

20

21   **Short Title:** The Syrian hamster SARS-CoV-2 infection model

22

23 **One Sentence Summary:** The Syrian hamster is highly susceptible to SARS-CoV-2 making it

24 an ideal infection model for COVID-19 countermeasure development.

25

26

27 **Abstract**

28 Following emergence in late 2019, SARS-CoV-2 rapidly became pandemic and is presently

29 responsible for millions of infections and hundreds of thousands of deaths worldwide. There is

30 currently no approved vaccine to halt the spread of SARS-CoV-2 and only very few treatment

31 options are available to manage COVID-19 patients. For development of preclinical

32 countermeasures, reliable and well-characterized small animal disease models will be of

33 paramount importance. Here we show that intranasal inoculation of SARS-CoV-2 into Syrian

34 hamsters consistently caused moderate broncho-interstitial pneumonia, with high viral lung loads

35 and extensive virus shedding, but animals only displayed transient mild disease. We determined

36 the infectious dose 50 to be only five infectious particles, making the Syrian hamster a highly

37 susceptible model for SARS-CoV-2 infection. Neither hamster age nor sex had any impact on

38 the severity of disease or course of infection. Finally, prolonged viral persistence in interleukin 2

39 receptor gamma chain knockout hamsters revealed susceptibility of SARS-CoV-2 to adaptive

40 immune control. In conclusion, the Syrian hamster is highly susceptible to SARS-CoV-2 making

41 it a very suitable infection model for COVID-19 countermeasure development.

42

43

Introduction

44

45 Since emergence of SARS-CoV-2 in late 2019, the virus has spread across the globe causing >31

46 million confirmed infections resulting in over 960,000 deaths. SARS-CoV-2 causes coronavirus

47 disease (COVID)-19, which is associated with a broad range of symptoms. These symptoms are

48 most commonly fever, dry cough and fatigue, but can also include myalgia, headache, loss of

49 taste or smell, sore throat, congestion, runny nose, nausea and diarrhea. The incubation period of

50 SARS-CoV-2 ranges from 2-14 days with 5-6 days being most common (1). While the majority

51 of infections are asymptomatic or present as mild to moderate cases, a small percentage of

52 patients will progress into acute respiratory disease with fatal outcome (2, 3). In the absence of a

53 licensed vaccine and only limited treatment options available, scientific and health care

54 communities continue their efforts to rapidly find effective countermeasures for SARS-CoV-2

55 infections. Aside from new drug or vaccine development, repurposing and 'off-label' use of

56 existing FDA-approved compounds is being heavily pursued, often omitting preclinical animal

57 studies before moving directly into humans (4-7).

58 Preclinical animal models are integral to evaluating countermeasures for infectious diseases such

59 as COVID-19. Non-human primate (NHP) COVID-19 models have been established, and

60 several Old-World monkey species have been shown to be susceptible to SARS-CoV-2

61 infection. Infection in these animals results in a transient mild to moderate interstitial pneumonia,

62 rather than the severe clinical outcomes (8-10). Ferrets have also been shown to be susceptible to

63 SARS-CoV-2 infection resulting in mild disease with shedding from the upper respiratory tract.

64 Efficient transmission has been documented suggesting the ferret may be a valuable preclinical

65 model for transmission but not for severe disease (11, 12).

66   Development of small animal SARS-CoV-2 infection models was initially delayed, but recently

67   both mouse and hamsters COVID-19 models have been described (13-17). The mouse

68   angiotensin-converting enzyme 2 (ACE-2) receptor has only low affinity for the SARS-CoV-2

69   spike protein leading to poor binding and entry (18, 19). Initially, mouse susceptibility to SARS-

70   CoV-2 infection was increased through transduction of the respiratory tract cells using

71   adenovirus vectors expressing human ACE2, which lead to development of non-lethal

72   pneumonia (20, 21). Several receptor transgenic mice have since been created, expressing human

73   ACE2 under tissue-specific promoters or the endogenous mouse ACE2 promoter (14, 22-24). All

74   of these mice are susceptible to SARS-CoV-2 infection, resulting in a range of clinical signs with

75   mild to fatal disease depending on the transgene. SARS-CoV-2 adaptation to mice has also been

76   attempted through either serial passaging or reverse genetics. So far this approach has sensitized

77   mice to infection, leading to very mild disease (13).

78   Syrian hamsters have been reported to be susceptible to SARS-CoV-2 infection developing

79   moderate interstitial pneumonia leading to transient mild to moderate disease (15, 17). However,

80   these studies have used varying doses of SARS-CoV-2 for inoculation, and the impact of age and

81   sex on infection and disease is unclear. Herein, we defined the Syrian hamster as a SARS-CoV-2

82   infection and disease model and refined further virologic and host parameters to increase the

83   value of this small animal model. First, we demonstrated high functional interaction of the

84   SARS-CoV-2 receptor binding domain (RBD) with the hamster ACE2 receptor. Next, we

85   determined the SARS-CoV-2 dose causing infection in 50% of animals (ID_{50}) following

86   intranasal infection, showing these animals to be highly susceptible to infection. We detailed the

87   progression of SARS-CoV-2 infection, and also the effect of sex and age on SARS-CoV-2

88   infection in the model. Finally, we investigated SARS-CoV-2 infection of interleukin 2 receptor,

89   gamma chain (*IL2RG*) knockout hamsters to assess the impact of adaptive (and NK) immunity in

90   this model.

91

92   **Materials and Methods**

93   **Biosafety and ethics.** All work using live SARS-COV-2 was performed in BSL4 using standard

94   operating protocols approved by the Rocky Mountain Laboratories Institutional Biosafety

95   Committee. All animal work was approved by the Institutional animal Care and use Committee

96   and performed in strict accordance with the recommendations described in the Guide for the

97   Care and Use of Laboratory Animals of the National Institutes of Health, the Office of Animal

98   Welfare, the United States Department of Agriculture in an association for Assessment and

99   Accreditation of Laboratory Animal Care-Accredited Facility. Animals were group housed in

100   HEPA-filtered cage systems enriched with nesting material. Commercial food and water were

101   available ad libitum.

102   **Virus.** SARS-CoV-2 isolate nCoV-WA1-2020 (MN985325.1) was kindly provided by CDC as

103   Vero passage 3 (25). The virus was propagated once in Vero E6 cells in DMEM (Sigma)

104   supplemented with 2% fetal bovine serum (Gibco), 1 mM L-glutamine (Gibco), 50 U/ml

105   penicillin and 50 µg/ml streptomycin (Gibco) (virus isolation medium). The used virus stock was

106   100% identical to the initial deposited Genbank sequence (MN985325.1) and no contaminants

107   were detected.

108   **Cells.** Vero E6 cells were maintained in DMEM (Sigma) supplemented with 10% fetal calf

109   serum (Gibco), 1 mM L-glutamine (Gibco), 50 U/ml penicillin and 50 µg/ml streptomycin

110   (Gibco). 293T and baby hamster kidney (BHK) were maintained in DMEM (Gibco)

111   supplemented with fetal bovine serum, penicillin/streptomycin and L-glutamine.

112   **Plasmids.** SARS-CoV-2 spike protein plasmids were previously described (18). Sequences from

113   SARS-CoV-1/Urbani spike (GenBank MN908947), SARS-CoV-2 spike RBD (AY278741),

114   human ACE2 (GenBank Q9BYF1.2) and hamster ACE2 (GenBank: XP_005074266.1) were

115   codon optimized for humans and cloned into pcDNA3.1+.

116   **Cell entry assay.** Vesicular stomatitis virus (VSV) particles were pseudotyped with different

117   wildtype or chimeric spike proteins or no spike in 293T cells as previously described (18). BHK

118   cells were transfected in 96-well format with 100 ng of host receptor plasmid, or no receptor and

119   subsequently infected with spike-pseudotyped VSV particles as previously described (18).

120   Approximately 18 hours later, luciferase was measured using the BrightGlo reagent (Promega),

121   following the manufacturer's instructions.

122   **Animal studies.** Syrian hamsters (*Mesocricetus auratus*), 6-8-weeks-of-age and >27-weeks-of-

123   age, males and females, were purchased from Envigo. *IL2RG* KO hamsters were generated with

124   CRISPR/Cas9-mediated gene targeting technique established in the hamster by Utah State

125   University as reported previously (26). Hamsters were anesthetized by inhalation of vaporized

126   isoflurane and inoculated via intranasal instillation with 50 μl of varying concentrations of

127   inoculum (1 to 1×10^5 tissue culture dose 50 ($TCID_{50}$) dropped into each naris (25ul/naris) using a

128   pipette. Hamsters were weighed and monitored daily for signs of disease. Temperature

129   transponders (BMDS IPTT-300) were implanted subcutaneously under anesthesia just above the

130   shoulder blades in a subset of hamsters to monitor and record temperatures daily. Swabs (oral

131   and rectal) were taken at different days post-infection using polyester flock tipped swabs (Puritan

132   Medical Products). Animals were euthanized for necropsies at different timepoints to assess

133   disease.

134   **Virus titration**. Virus was quantified through end-point titrations performed in Vero E6 cells.

135   Tissue was homogenized in 1ml DMEM using a TissueLyzer (Qiagen) and centrifuged to

136   remove cellular debris (10 minutes at 8,000 rpm). Cells were inoculated with 10-fold serial

137   dilutions of clarified tissue homogenate or whole blood samples in 100 µl DMEM (Sigma-

138   Aldrich) supplemented with 2% fetal bovine serum, 1 mM L-glutamine, 50 U/ml penicillin and

139   50 µg/ml streptomycin. Cells were incubated for seven days and then scored for cytopathic effect

140   (CPE). The $TCID_{50}$ was calculated via the Reed-Muench formula (27).

141   **Viral genome load.** qRT-PCR was performed on RNA extracted from blood and swabs using

142   QiaAmp Viral RNA kit (Qiagen) according to the manufacturer's instructions. Tissues (≤ 30 mg)

143   were homogenized in RLT buffer and RNA was extracted using the RNeasy kit (Qiagen)

144   according to the manufacturer protocol. Viral genomic RNA (gRNA) was detected with a one-

145   step real-time RT-PCR assay (Quantifast, Qiagen) using primers and probes generated to target

146   either the SARS-CoV-2 E (28) or N gene (forward: 5'- AGAATGGAGAACGCAGTGGG;

147   reverse: 5'- TGAGAGCGGTGAACCAAGAC; probe: 5'-CGATCAAAACAACGTCGGCC

148   synthesized with 5' 6-carboxyfluorescein, internal Zen quencher and 3' Iowa black quencher);

149   all primers and probes were synthesized by Integrated DNA Technologies (IDT). Dilutions of

150   RNA standards quantified by droplet digital PCR were run in parallel and used to calculate

151   gRNA copies with the E assay. The N-based assay used a standard curve synthesized as follows:

152   T7 *in vitro* transcription (ThermoFisher) of a synthetically produced N sequence (IDT) was used

153   to generate template RNA. RNA was quantified by 260nm absorbance to determine copy number

154   and a standard curve generated by serial dilution.

155   **Histopathology and immunohistochemistry.** Tissues were fixed in 10% neutral buffered

156   formalin (with two changes) for a minimum of 7 days. Tissues were placed in cassettes and

157   processed with a Sakura VIP-6 Tissue Tek on a 12-hour automated schedule, using a graded

158   series of ethanol, xylene, and ParaPlast Extra. Embedded tissues are sectioned at 5um and dried

159   overnight at 42°C prior to staining. Specific anti-CoV immunoreactivity was detected using

160   GenScript U864YFA140-4/CB2093 NP-1 at a 1:1,000 dilution. The secondary antibody is an

161   anti-rabbit IgG polymer from Vector Laboratories ImPress VR. Tissues were then processed for

162   immunohistochemistry using the Discovery Ultra automated processor (Ventana Medical

163   Systems) with a ChromoMap DAB kit (Roche Tissue Diagnostics).

164   **Statistical analyses.** Statistical analysis was performed in Prism 8 (GraphPad). T-tests were used

165   to assess studies with 2 groups, ANOVA was used to analyze studies with >2 groups.

166

167   **Results**

168   **The SARS-CoV-2 spike protein binds to the Syrian hamster ACE2 receptor**. To validate that

169   that SARS-CoV-2 can bind and then use as an entry receptor the Syrian hamster ACE2 receptor,

170   a VSV pseudotype assay was performed as previously published (18). Briefly, a chimeric SARS-

171   CoV-1 spike protein was generated with the RBD replaced with the SARS-CoV-2 RBD (VSV-

172   SARS-CoV-2-RBD) (18). We transfected BHK cells that do not express ACE2 with expression

173   plasmids for either human or hamster ACE2, or empty vector as a negative control. Cells were

174   then infected with the VSV pseudotyped particles carrying either SARS-CoV-1 full-length spike

175   (VSV-SARS-CoV-1-RBD) or chimeric VSV-SARS-CoV-2-RBD. As anticipated, both VSV-

176   SARS-COV-1-RBD and VSV-SARS-CoV-2-RBD were unable to enter BKH cells, but entry

177   was rescued in transduced cells expressing the hamster or human ACE2. Interestingly, VSV-

178   SARS-CoV-2-RBD entry was increased compared to VSV-SARS-CoV-1-RBD, independent of

179   the ACE2 origin, which may indicate higher susceptibility of both hamsters and humans to

180   SARS-CoV-2 compared to SARS-CoV-1 (Fig. 1).

181   **Syrian hamsters are highly susceptible to SARS-CoV-2.** To determine the level of

182   susceptibility of Syrian hamsters to SARS-CoV-2 infection, four groups of six hamsters aged 4-6

183   weeks were infected with limiting dilutions of SARS-CoV-2 to determine the ID_{50}. Groups were

184   intranasally infected with a ten-fold serial dilution series of virus ranging from 10^3 to 10^0

185    $TCID_{50}$, and infection course was monitored by signs of disease including weight and

186   temperature. Although no significant changes in temperature over the experimental period were

187   observed, weight loss between the animal groups directly correlated with the infectious dose

188   (Fig. 2A). Oral and rectal swabs were taken at 3 days post infection (dpi) and 5dpi to measure

189   differences in levels of viral gRNA between the different groups. Only one animal in the group

190   receiving the 1 $TCID_{50}$ dose had detectable gRNA in the oral swabs and none in the rectal swab

191   (Fig. 2B), with only half the animals in this group being positive at 5dpi (Fig. 2C). Lungs were

192   harvested at 5dpi and gRNA and infectious titers were determined. Remarkably similar gRNA

193   levels were found across groups infected with 10 $TCID_{50}$ or higher, only the 1 $TCID_{50}$ group had

194   a significant reduction in gRNA levels (Fig. 2D). Infectious titers from the lungs of each dose

195   group had a similar pattern with high viral loads in all groups, except the 1 $TCID_{50}$ group for

196   which no infectious virus was detected (Fig. 2E). Remarkably, this series of experiments shows

197   the ID_{50} in Syrian hamsters to be only 5 $TCID_{50}$ when administered intranasally.

198   **SARS-CoV-2 infection of Syrian hamsters results in broncho-interstitial pneumonia.** To

199   characterize the extent of disease in this model, two groups of 10 Syrian hamsters aged 4-6

200   weeks were intranasally infected with either 500 ID_{50} (low dose; 10^3 $TCID_{50}$) or $5x10^4$ ID_{50} (high

201   dose; 10^5 $TCID_{50}$) of SARS-CoV-2. Animals were monitored for clinical symptoms of disease

202   with the intent of euthanizing a subset of animals for analysis when early symptoms became

203   apparent. At 3dpi hamsters in both groups had lost weight on consecutive days (Fig. 3A) and

204   displayed slightly ruffled fur with minor changes in respiration pattern. Four animals from each

205   group were euthanized at this time (3dpi) for analysis. Lungs were examined for gross pathology

206   and all animals had lung lesions consisting of focal extensive areas of pulmonary edema and

207   consolidation with evidence of interstitial pneumonia characterized by a failure of the lungs to

208   collapse following removal. No gross pathology was observed in other tissues collected

209   including liver, spleen, kidney and brain. The remaining hamsters continued to lose weight until

210   5dpi with a maximum loss of <10% body weight (Fig. 3A); clinical signs remained similar until

211   5dpi. Three more animals from each group were euthanized at this time (5dpi). At necropsy, an

212   increase in both number and severity of lesions were observed in animals receiving the low dose,

213   but gross pathology was similar in appearance at 3dpi and 5dpi in animals receiving the high

214   dose. Following four consecutive days of weight gain (Fig. 3A) and improving clinical signs, the

215   remaining animals from each group were euthanized at 10dpi. Gross examination of the lungs at

216   10dpi showed a significant reduction in both lesion severity and congestion relative to lungs

217   taken earlier during disease progression. Despite the obvious development of respiratory disease

218   at earlier times post-infection, clinical signs were minimal at this stage (10dpi) with animals

219   having recovered weight (Fig. 3A). Oral and rectal swabs were collected at each time point to

220   monitor viral gRNA shedding. Shedding peaked in all swab types at 3dpi with a small decrease

221   at 5dpi before dropping significantly at 10dpi (Fig. 3B, C). Lungs were evaluated for both

222   SARS-CoV-2 gRNA and infectious titers. gRNA loads in the lungs were high with >10^{10}

223 genome copies/gram (Fig. 3D), whereas gRNA loads in other organs were approximately 4-5

224 logs lower (Sup. Fig. 1). Lung infectious titers were 10^7 $TCID_{50}$ per gram at 3dpi although this

225 had already decreased at 5dpi and was absent in all but one animal at 10dpi (Fig. 3E). Overall,

226 there was no significant difference between the groups infected with the low and high dose of

227 SARS-CoV-2, except for 10dpi where one animal remained positive.

228 Pathologically, changes associated with disease in the lower respiratory tract were noted in both

229 the trachea and lung regardless of the inoculation dose. The observed pathology had a more

230 distinct progression in the low (500 ID_{50}) inoculation dose than the higher dosed group ($5x10^4$

231 ID_{50}). Evidence of broncho-interstitial pneumonia was observed at all evaluated time points. At

232 3dpi, lesions were characterized by epithelial necrosis in the trachea and bronchioles, squamous

233 metaplasia of the mucosa in the trachea, bronchiolitis characterized by influx of neutrophils and

234 macrophages into the lamina propria and mild interstitial pneumonia with expansion of alveolar

235 septa by edema fluid, with few strands of fibrin and low numbers of leukocytes (Fig 4. A-C). By

236 5dpi, the interstitial pneumonia was moderate to severe with fibrin leaking into alveolar spaces,

237 alveolar edema, influx of moderate numbers to numerous neutrophils and macrophages into

238 alveolar spaces, presence of syncytial cells in bronchioles and alveolar spaces and prominent

239 type II pneumocyte hyperplasia (Fig. 4D-F). Evidence of lesion resolution was observed at 10dpi

240 with a decrease in alveolar cellular exudate, absence of epithelial necrosis and a prominent

241 "honeycombing" pattern of type II pneumocyte hyperplasia centered on terminal bronchioles

242 with septal expansion by a small to moderate amount of fibrosis (Fig. 4G-I). Mild and multifocal

243 pleural fibrosis was observed at 10dpi (Fig. 5). At both 5dpi and 10dpi, moderate numbers of

244 blood vessels were surrounded by perivascular infiltrates of lymphocytes that frequently formed

245 distinct perivascular cuffs, occasionally focally disrupting the tunica media or forming

246   aggregates between the tunica intima and media elevating the endothelium into the lumen.

247   Immunohistochemical reaction demonstrated viral antigen in bronchiole epithelial cells at 3dpi

248   (Fig. 5A-C) with fewer cells showing immunoreactivity at 5dpi (Fig. 5D-E) and no epithelial

249   cells exhibiting immunoreactivity at 10dpi (Fig. 5G-I). Lower in the respiratory tree, SARS-

250   CoV-2 immunoreactivity was demonstrated in type I and II pneumocytes as well as alveolar

251   macrophages at 3dpi and 5dpi with a lack of immunoreactivity at 10dpi (Fig. 5G-I). Overall,

252   pathologic changes progressed more rapidly in animals infected with the high dose relative to the

253   low dose, but severity of disease was consistent between the groups with all animals developing

254   moderate to severe broncho-interstitial pneumonia, commensurate with a mild to moderate

255   infection model.

256   **Neither age nor gender affected disease severity or outcome.** To determine whether age or

257   gender would affect disease progression following SARS-CoV-2 infection, we infected both

258   young (4-6 weeks old) and aged (>6 months old) male and female hamsters with the low dose of

259   500 ID_{50} (10^3 $TCID_{50}$) by the intranasal route. Consistent with previous studies, animals began to

260   show mild clinical signs of disease and weight loss peaking at 5dpi or 6dpi (Fig. 6A). A subset of

261   animals in each age group and gender were euthanized for analysis at 3, 5 and 11dpi. Lung

262   pathology was comparable in all groups at each time point throughout the study. Gross lung

263   lesions were evident at 3dpi, had worsened by 5dpi before mostly resolving at 11dpi (Supp. Fig.

264   2A). To help determine disease severity, lung weights were recorded and calculated as a

265   percentage of overall body weight for comparison. Lungs weights paralleled the observed lesions

266   and were significantly increased at 5dpi (Supp. Fig. 2B). These observations were consistent

267   with the development of pneumonia and was independent of sex and age.

268 High levels of viral gRNA were detected in oral and rectal swabs in all groups. The highest

269 gRNA levels detected were 3dpi before decreasing at 5dpi and again at 11dpi where only a

270 subset remained positive (Fig. 6B, C). Interestingly, all oral swabs were positive at 11dpi

271 suggesting viral replication was still ongoing in the upper respiratory areas (Fig. 6B). Several

272 tissues including blood were collected and examined by qRT-PCR for viral gRNA loads at each

273 timepoint. The lungs had high viral loads with gRNA levels highest 3dpi before decreasing at

274 5dpi and again at 11dpi (Fig. 6D). This corresponded with infectious titers which followed a

275 similar pattern and peaked at 3dpi (Fig. 6E). The brain consistently had the second highest levels

276 of viral gRNA detected and remained relatively stable across the groups at $>10^8$ TCID$_{50}$

277 equivalents at the time points examined. The digestive tract, both upper and lower, exhibited

278 levels of gRNA of $>10^6$ TCID$_{50}$ equivalents across the study. Liver, spleen and kidneys all had

279 similar levels of gRNA at 3dpi and 5dpi with $>10^4$ TCID$_{50}$ equivalents before decreasing at

280 11dpi.

281 **Hamsters lacking interleukin-2 receptor subunit gamma (*IL2RG* KO) show persistent**

282 **infection with SARS-CoV-2.** *IL2RG* KO hamsters are unable to develop mature NK cells with

283 compromised development of T and B lymphocytes (26, 29). This lack of mature lymphoid cells

284 results in an immunocompromised status known as X-linked severe combined immunodeficiency

285 (XSCID) in humans (30). To ask the question of whether these key cellular aspects of the innate

286 (NK) and adaptive (B and T cells) impact SARS-CoV-2 replication and associated disease, we

287 assessed infection in *IL2RG* KO hamsters. Similar to immunocompetent Syrian hamsters,

288 following infection with 5×10^4 ID$_{50}$ (high dose; 10^5 TCID$_{50}$) of SARS-CoV-2, four (2 males, 2

289 females) *IL2RG* KO hamsters lost approximately 5-10% of their body weight over the first 5

290 days following infection before recovering (Fig. 7A). Oral and rectal swabs were taken at 5dpi

291 and 24dpi to measure shedding. Interestingly, both oral and rectal swabs were positive at both

292 time-points and at very similar levels (Fig. 7B). All four hamsters were euthanized 24dpi

293 following 2 weeks of consistent weight gain and lungs were examined for disease. At

294 examination, the lungs had lesions similar to the immunocompetent hamsters at 5dpi, were

295 congested and failed to collapse. Remarkably, virus titration performed on lung tissue revealed

296 high infectious titers ranging from 10^7 - 10^9 TCID$_{50}$ per gram of tissue, even at 24dpi (Fig. 7C).

297 Histopathologic analysis of the lung sections of all evaluated *IL2RG* KO hamsters exhibited

298 disseminated, moderate to severe, chronic-active interstitial pneumonia. Alveolar septa were

299 expanded by moderate amounts of fibrin, variably well-organized bundles of collagen and

300 infiltrated by moderate numbers of neutrophils and macrophages. Adjacent alveolar spaces

301 frequently contained moderate numbers to numerous macrophages with fewer degenerate and

302 non-degenerate neutrophils admixed with cellular debris (Fig. 7D). Greater than 50% of

303 evaluated alveolar spaces were lined by type II pneumocytes that occasionally exhibited pseudo-

304 stratified, columnar epithelial differentiation with a distinct ciliated apical border. Lymphocyte

305 infiltrates and perivascular lymphoid aggregates were absent in all evaluated sections.

306 Immunohistochemical reaction revealed numerous immunoreactive type I and type II

307 pneumocytes as well as immunoreactive ciliated bronchiolar epithelial cells (Fig. 7E).

308 Histopathologic evaluation of the spleen confirmed the absence of lymphoid follicles and peri-

309 arteriolar lymphoid sheaths. Extramedullary hematopoiesis, noted in both the spleen and liver,

310 consisted entirely of erythroid lineage cell populations.

311

312 **Discussion**

313   SARS-CoV-2 infection in humans varies from asymptomatic to severe respiratory disease that

314   can be fatal, especially in elderly and otherwise immunocompromised individuals. The lack of

315   preclinical animal models that replicate the severe disease of some COVID-19 patients is a

316   substantial hurdle for the progression of promising countermeasures from in vitro testing through

317   to clinical trials. A reliable small animal model would allow reproducible, in-depth analyses of

318   infection patterns, elucidation of the immune response to SARS-CoV-2 infection and serve as a

319   critical preclinical model for the initial in vivo step in evaluating COVID-19 countermeasures for

320   human use.

321   The Syrian hamster has been established as a SARS-CoV-2 animal model, but a more thorough

322   analysis had yet to be performed. To expand our understanding the Syrian hamster model, we

323   first determined that the hamster ACE2 receptor was compatible with the SARS-CoV-2 spike

324   protein binding domain. The level of binding and entry was consistently higher than the

325   corresponding assay testing human ACE2 binding activity. As the receptor binding data

326   suggested and other recent studies have shown, Syrian hamsters were susceptible to SARS-CoV-

327   2 infection resulting in moderate to severe broncho-interstitial pneumonia and prolonged virus

328   shedding of at least 10 days. The ID_{50} of SARS-CoV-2 in the Syrian hamster is low, roughly five

329   infectious particles will result in a productive infection in 50% of animals.

330   Symptoms of disease appear approximately 3dpi, but clinical signs are minimal with a consistent

331   but not severe weight loss of 5-10%. Ruffled fur may be observed in some hamsters, respiration

332   rates may increase slightly, but the behavior is unchanged from naïve hamsters. Infection was

333   systemic following intranasal inoculation and viral gRNA was detected in all tissues examined.

334   However, the lungs were the major site of viral replication and clearly showed a consistent but

335   moderate pathology. Following intranasal infection, interstitial pneumonia initiating as

336 bronchiolitis and focusing around terminal airways developed at 3dpi but was more severe in the

337 animals receiving higher infectious doses at this early time point. Pulmonary pathology

338 continued to increase in severity and extent of lesions in the lower dosed animals and was more

339 severe at 5dpi, with characteristic evidence of coronaviral infection noted including presence of

340 syncytial cells in bronchioles and alveolar spaces. Pulmonary pathology was diminished by

341 10dpi in all animals examined at those times with characteristic evidence of epithelial

342 regeneration noted.

343 In the human population, there have been reports of an increase in COVID-19 severity in males

344 (31, 32) as well as a disparity of COVID-19 severity among different age groups (33, 34). In

345 these studies, neither age nor gender was a factor in disease severity or outcome. Young

346 hamsters had similar shedding kinetics, virus titers in the lungs and developed similar pulmonary

347 pathology as aged hamsters regardless of sex. Importantly, all animals taken at the late

348 timepoints showed evidence of recovery from disease at a similar rate.

349 Interestingly, elimination of host adaptive immune responses in the *IL2RG* KO model resulted in

350 a chronic infection persisting at least 24 days. Virus was detectable in oral and rectal swabs at

351 5dpi and at study termination (24dpi). Histopathology evaluated at 24dpi supports a chronic-

352 active infection of the respiratory system with foci of epithelial regeneration as well as active

353 recruitment of neutrophils and macrophages. Unlike the immunocompetent hamster model, in

354 which antigen was only detectable outside of regions of pathology, SARS-CoV-2 antigen was

355 detectable in type I and type II pneumocytes, hyperplastic pneumocytes in regions of

356 regeneration and macrophages. Additionally, viral antigen was present in morphologically

357 normal bronchial epithelial cells at 24dpi, a feature only routinely observed at 3dpi in the

358 immunocompetent hamster model. While histopathology revealed a moderate to severe

359   pulmonary inflammatory response, clinical signs of severe respiratory disease was not observed

360   in this model. These data suggest that the innate immune system, in the background of

361   compromised adaptive immunity, is capable of depressing the viral infection enough to keep

362   respiratory physiology relatively stable, but incapable of eliminating SARS-CoV-2 infection.

363   Additionally, vascular changes and perivascular leukocyte infiltrates were not observed in the

364   *IL2RG* KO model, unlike the immunocompetent hamster model. This data, even though limited

365   to four animals, suggests that the adaptive immune response or IL-2 signaling pathway may play

366   a critical role in the development of innate leukocyte recruitment and staging during viral

367   infection and the regulation of the coagulation cascade in response to a pro-inflammatory local

368   environment.

369   Both autopsy and terminal biopsy samples from human patients exhibiting COVID-19 disease

370   have shown histologic evidence of diffuse alveolar disease, and death is frequently attributed to

371   the clinical progression of pneumonia, often times resulting in acute respiratory distress. Diffuse

372   alveolar disease in SARS-CoV-2 infection has characteristic lesions of hyaline membrane

373   formation in alveolar spaces accompanied with proteinaceous fluid leaking from damaged

374   vessels into alveolar spaces. In hamsters, there is evidence of alveolar epithelial damage at peak

375   virus replication with lesion resolution later on. However, the hamster model fails to develop

376   fulminant diffuse alveolar disease and lacks the respiratory decompensation associated with the

377   clinical syndrome of acute respiratory distress. Relative to the recently developed NHP models

378   (8, 10), the Syrian hamster model exhibits a similar mild disease phenotype and is well suited for

379   assessing therapeutics or vaccines.

380   Another effective small animal model of COVID-19, the human ACE2 mouse, show these

381   animals develop pneumonia resulting in fatal disease following SARS-CoV-2 infection (14, 24,

382   35). However, with this mouse model there is concern about the location and level of receptor

383   expression in these human ACE2 transgenic mice. The increase in expression locales and levels

384   could result in enhanced or systemic disease dissimilar to COVID-19 in humans as these animals

385   have been reported to develop fatal encephalitis (35), a clinical manifestation not currently

386   associated with severe COVID-19 disease in humans. Additionally, the human ACE2 mouse has

387   been previously shown to cause neuronal death without evidence of encephalitis in the SARS-

388   CoV-1 model (36). These complications may limit therapeutic studies in the human ACE2

389   mouse model.

390   Although, as with all animal models, there are some limitations exemplified by the lack of a

391   systemic response to SARS-CoV-2 infection. The only mild disease manifestation and ability to

392   quickly limit the infection make this model less suitable to study the mechanisms of severe

393   COVID-19. However, the consistent and easily measured lung disease found in hamsters of all

394   ages and sex make this a suitable infection model to evaluate SARS-CoV-2 countermeasure

395   development.

396

397   **Acknowledgements**

404

Conflict of Interest

406   The authors do not declare any conflict of interest.

407

DISCLAIMER

409   The opinions, conclusions and recommendations in this report are those of the authors and do not

410   necessarily represent the official positions of the National Institute of Allergy and Infectious

411   Diseases (NIAID) at the National Institutes of Health (NIH).

412

References

414   1.   CDC COVID Data Tracker 2020 [cited 2020 September 23, 2020]. Maps, Charts and
415   Data]. Available from: https://covid.cdc.gov/covid-data-tracker/#cases_casesinlast7days.
416   2.   Chen N, Zhou M, Dong X, Qu J, Gong F, Han Y, et al. Epidemiological and clinical
417   characteristics of 99 cases of 2019 novel coronavirus pneumonia in Wuhan, China: a descriptive
418   study. Lancet. 2020;395(10223):507-13.
419   3.   Wang D, Hu B, Hu C, Zhu F, Liu X, Zhang J, et al. Clinical Characteristics of 138
420   Hospitalized Patients With 2019 Novel Coronavirus-Infected Pneumonia in Wuhan, China.
421   JAMA. 2020.
422   4.   Gautret P, Lagier JC, Parola P, Hoang VT, Meddeb L, Mailhe M, et al. Hydroxychloroquine
423   and azithromycin as a treatment of COVID-19: results of an open-label non-randomized clinical
424   trial. Int J Antimicrob Agents. 2020:105949.
425   5.   Sanders JM, Monogue ML, Jodlowski TZ, Cutrell JB. Pharmacologic Treatments for
426   Coronavirus Disease 2019 (COVID-19): A Review. JAMA. 2020;323(18):1824-36.
427   6.   Ali MJ, Hanif M, Haider MA, Ahmed MU, Sundas F, Hirani A, et al. Treatment Options for
428   COVID-19: A Review. Frontiers in Medicine. 2020;7(480).
429   7.   Jarvis MA, Hansen FA, Rosenke K, Haddock E, Rollinson C, Rule S, et al. Evaluation of
430   drugs for potential repurposing against COVID-19 using a tier-based scoring system. Antivir
431   Ther. 2020.

432   8.   Munster VJ, Feldmann F, Williamson BN, van Doremalen N, Pérez-Pérez L, Schulz J, et al.
433   Respiratory disease in rhesus macaques inoculated with SARS-CoV-2. Nature. 2020.
434   9.   Finch CL, Crozier I, Lee JH, Byrum R, Cooper TK, Liang J, et al. Characteristic and
435   quantifiable COVID-19-like abnormalities in CT- and PET/CT-imaged lungs of SARS-CoV-2-
436   infected crab-eating macaques (Macaca fascicularis). bioRxiv. 2020.
437   10.   Rockx B, Kuiken T, Herfst S, Bestebroer T, Lamers MM, Oude Munnink BB, et al.
438   Comparative pathogenesis of COVID-19, MERS, and SARS in a nonhuman primate model.
439   Science. 2020;368(6494):1012-5.
440   11.   Kim YI, Kim SG, Kim SM, Kim EH, Park SJ, Yu KM, et al. Infection and Rapid Transmission
441   of SARS-CoV-2 in Ferrets. Cell Host Microbe. 2020;27(5):704-9.e2.
442   12.   Schlottau K, Rissmann M, Graaf A, Schon J, Sehl J, Wylezich C, et al. SARS-CoV-2 in fruit
443   bats, ferrets, pigs, and chickens: an experimental transmission study. Lancet Microbe. 2020.
444   13.   Dinnon KH, Leist SR, Schäfer A, Edwards CE, Martinez DR, Montgomery SA, et al. A
445   mouse-adapted SARS-CoV-2 model for the evaluation of COVID-19 medical countermeasures.
446   bioRxiv. 2020:2020.05.06.081497.
447   14.   Bao L, Deng W, Huang B, Gao H, Liu J, Ren L, et al. The pathogenicity of SARS-CoV-2 in
448   hACE2 transgenic mice. Nature. 2020.
449   15.   Imai M, Iwatsuki-Horimoto K, Hatta M, Loeber S, Halfmann PJ, Nakajima N, et al. Syrian
450   hamsters as a small animal model for SARS-CoV-2 infection and countermeasure development.
451   Proc Natl Acad Sci U S A. 2020.
452   16.   Gu H, Chen Q, Yang G, He L, Fan H, Deng Y-Q, et al. Rapid adaptation of SARS-CoV-2 in
453   BALB/c mice: Novel mouse model for vaccine efficacy. bioRxiv. 2020:2020.05.02.073411.
454   17.   Sia SF, Yan LM, Chin AWH, Fung K, Choy KT, Wong AYL, et al. Pathogenesis and
455   transmission of SARS-CoV-2 in golden hamsters. Nature. 2020.
456   18.   Letko M, Marzi A, Munster V. Functional assessment of cell entry and receptor usage for
457   SARS-CoV-2 and other lineage B betacoronaviruses. Nat Microbiol. 2020;5(4):562-9.
458   19.   Wan Y, Shang J, Graham R, Baric RS, Li F. Receptor Recognition by the Novel Coronavirus
459   from Wuhan: an Analysis Based on Decade-Long Structural Studies of SARS Coronavirus. Journal
460   of Virology. 2020;94(7):e00127-20.
461   20.   Hassan AO, Case JB, Winkler ES, Thackray LB, Kafai NM, Bailey AL, et al. A SARS-CoV-2
462   Infection Model in Mice Demonstrates Protection by Neutralizing Antibodies. Cell. 2020.
463   21.   Israelow B, Song E, Mao T, Lu P, Meir A, Liu F, et al. Mouse model of SARS-CoV-2 reveals
464   inflammatory role of type I interferon signaling. bioRxiv. 2020:2020.05.27.118893.
465   22.   McCray PB, Jr., Pewe L, Wohlford-Lenane C, Hickey M, Manzel L, Shi L, et al. Lethal
466   infection of K18-hACE2 mice infected with severe acute respiratory syndrome coronavirus. J
467   Virol. 2007;81(2):813-21.
468   23.   Tseng CT, Huang C, Newman P, Wang N, Narayanan K, Watts DM, et al. Severe acute
469   respiratory syndrome coronavirus infection of mice transgenic for the human Angiotensin-
470   converting enzyme 2 virus receptor. J Virol. 2007;81(3):1162-73.
471   24.   Sun SH, Chen Q, Gu HJ, Yang G, Wang YX, Huang XY, et al. A Mouse Model of SARS-CoV-
472   2 Infection and Pathogenesis. Cell Host Microbe. 2020.
473   25.   Harcourt J, Tamin A, Lu X, Kamili S, Sakthivel SK, Murray J, et al. Severe Acute
474   Respiratory Syndrome Coronavirus 2 from Patient with 2019 Novel Coronavirus Disease, United
475   States. Emerg Infect Dis. 2020;26(6).

476   26.   Li R, Ying B, Liu Y, Spencer JF, Miao J, Tollefson AE, et al. Generation and characterization
477   of an IL2RG knockout Syrian hamster model for XSCID and HAdV-C6 infection in
478   immunocompromised patients. Dis Model Mech. 2020.
479   27.   REED LJ, MUENCH H. A SIMPLE METHOD OF ESTIMATING FIFTY PER CENT ENDPOINTS12.
480   American Journal of Epidemiology. 1938;27(3):493-7.
481   28.   Corman VM, Landt O, Kaiser M, Molenkamp R, Meijer A, Chu DK, et al. Detection of
482   2019 novel coronavirus (2019-nCoV) by real-time RT-PCR. Euro Surveill. 2020;25(3).
483   29.   Leonard WJ, Lin JX, O'Shea JJ. The gammac Family of Cytokines: Basic Biology to
484   Therapeutic Ramifications. Immunity. 2019;50(4):832-50.
485   30.   Allenspach E, Rawlings DJ, Scharenberg AM. X-Linked Severe Combined
486   Immunodeficiency. In: Adam MP, Ardinger HH, Pagon RA, Wallace SE, Bean LJH, Stephens K, et
487   al., editors. GeneReviews((R)). Seattle (WA)1993.
488   31.   La Vignera S, Cannarella R, Condorelli RA, Torre F, Aversa A, Calogero AE. Sex-Specific
489   SARS-CoV-2 Mortality: Among Hormone-Modulated ACE2 Expression, Risk of Venous
490   Thromboembolism and Hypovitaminosis D. Int J Mol Sci. 2020;21(8).
491   32.   Conti P, Younes A. Coronavirus COV-19/SARS-CoV-2 affects women less than men:
492   clinical response to viral infection. J Biol Regul Homeost Agents. 2020;34(2).
493   33.   Grasselli G, Zangrillo A, Zanella A, Antonelli M, Cabrini L, Castelli A, et al. Baseline
494   Characteristics and Outcomes of 1591 Patients Infected With SARS-CoV-2 Admitted to ICUs of
495   the Lombardy Region, Italy. Jama. 2020;323(16):1574-81.
496   34.   Park SE. Epidemiology, virology, and clinical features of severe acute respiratory
497   syndrome -coronavirus-2 (SARS-CoV-2; Coronavirus Disease-19). Clin Exp Pediatr.
498   2020;63(4):119-24.
499   35.   Jiang RD, Liu MQ, Chen Y, Shan C, Zhou YW, Shen XR, et al. Pathogenesis of SARS-CoV-2
500   in Transgenic Mice Expressing Human Angiotensin-Converting Enzyme 2. Cell. 2020.
501   36.   Netland J, Meyerholz DK, Moore S, Cassell M, Perlman S. Severe acute respiratory
502   syndrome coronavirus infection causes neuronal death in the absence of encephalitis in mice
503   transgenic for human ACE2. J Virol. 2008;82(15):7264-75.

504

505   **Figure legends**

506   **Figure 1: SARS-CoV-2 spike receptor binding data.** A VSV pseudotype assay was used to

507   assess the binding affinity of the SARS-CoV-2 RBD. BHK cells expressing either the human or

508   Syrian hamster or no ACE2 receptor were infected with VSV-pseudotyped particles carrying

509   either the SARS-CoV-1 spike (S) protein or a chimeric SARS-CoV-1 spike with the SARS-CoV-

510   2 receptor binding domain (RBD). *Note:* red circles, SARS-CoV-1 S; yellow circles with red

511   outline, SARS-CoV-1 S with SARS-CoV-2 RBD; black circle, no ACE-2; S, spike protein;

512   RBD, receptor binding domain.

513   **Figure 2: Susceptibility of Syrian hamsters to SARS-CoV-2.** Syrian hamsters were inoculated

514   intranasally with 10-fold limiting dilutions of SARS-CoV-2 beginning at 10^3 TCID$_{50}$. Weights

515   were collected daily and shedding was assessed via swab samples (nasal and rectal) collected at

516   3dpi and 5dpi. Viral loads were determined as genome copies and infectious virus. (A) Daily

517   weights. (B) Shedding at 3dpi. (C) Shedding at 5dpi. (D) Viral genome load in the lungs at 5dpi.

518   (E) Infectious lung titers at 5dpi. A statistical significance was found between the groups

519   presented in (A), with the group receiving the highest dose of 10^3 TCID$_{50}$ losing the most weight.

520   The group receiving the second highest infectious dose (10^2 TCID$_{50}$) lost statistically less than

521   the 10^3 TCID$_{50}$ group but statistically more weight than the 2 groups receiving the two lowest

522   infectious doses. (B-E) A statistically significance difference was found between the group

523   receiving the lowest dose (10^0 TCID$_{50}$) and all other groups. Multiple t tests comparing groups

524   directly were used to analyze significance. *Note:* blue circles, 10^0 TCID$_{50}$ dose; red square, 10^1

525   TCID$_{50}$ dose; green triangle, 10^2 TCID$_{50}$ dose; purple triangle, 10^3 TCID$_{50}$ dose.

526   **Figure 3: Increased infectious dose does not affect shedding or disease severity.** Syrian

527   hamsters were infected intranasally with either 500 ID$_{50}$ (10^3 TCID$_{50}$) or 5x10^4 ID$_{50}$ (10^5 TCID$_{50}$)

528   of SARS-CoV-2. Samples were collected at the time points noted. Weight were collected daily,

529   shedding from mucosal membranes and viral genome load and infectivity in the lungs were

530   measured. (A) Daily weights. (B) Viral genome load recovered from nasal swabs. (C) Viral

531   genome load recovered from rectal swabs. (D) Viral genome load in the lungs. (E) Infectious

532   titers in the lungs. T-tests were used to compare the two groups at each time where samples were

533   collected. A significant difference was observed at 10dpi in the lung titers (E), but no other

534   significant differences were observed in this study. *Note:* blue circles, 10^5 TCID$_{50}$ dose; red

535   square, 10^3 TCID$_{50}$ dose.

536   **Figure 4: SARS-CoV-2 infection of Syrian hamsters results in broncho-interstitial**

537   **pneumonia.** Syrian hamsters were infected intranasally with 500 ID$_{50}$ (10^3 TCID$_{50}$) of SARS-

538   CoV-2. Lungs were fixed in 10% formalin, cut and stained with Hematoxylin and Eosin (HE) to

539   examine pulmonary pathology at 3, 5 and 10dpi. (A-C), 3dpi. (A) Inflammation initiates within

540   interstitial spaces in and around terminal airways with a minimal cellular exudate into the airway

541   spaces (100x, size bar is 50um). (B) Bronchiolar epithelial necrosis with influx of neutrophils

542   into the mucosa and airway lumen (400x, size bar is 20um). (C) Attenuation of the tracheal

543   mucosa with loss of apical cilia accompanied with an influx of moderate numbers of degenerate

544   and non-degenerate neutrophils (400x, size bar is 20um). (D-F), 5dpi. (D) Locally extensive

545   inflammation is noted (100x, size bar is 50um). (E) Progressive bronchiolitis with degenerate

546   and non-degenerate neutrophils and exudate within the lumen and prominent epithelial syncytial

547   cells (arrows; 400x, size bar is 20um). (F) Alveolar spaces contain macrophages and neutrophils.

548   Alveolar septa are thickened and expanded by fibrin, edema fluid and infiltrating leukocytes and

549   are lined by prominent type II pneumocytes (arrowhead) and rare syncytial cells (arrow; 400x,

550   size bar is 20um). (G-I), 10dpi. (G) Resolving inflammation is largely limited to bronchioles and

551   the adjacent alveolar spaces (100x, size bar is 50um) (H) Alveolar septa are thickened by

552   collagen with lymphocytes and lined by numerous plump type II pneumocytes that surround low

553   numbers of foamy alveolar macrophages (400x, size bar is 20um). (I) Multifocal pleural fibrosis

554   is evident with mild subpleural inflammation (200x, size bar is 20um).

555   **Figure 5: SARS-CoV-2 viral antigen in the lungs over the course of infection.** Syrian

556   hamsters were infected intranasally with 500 ID$_{50}$ (10^3 TCID$_{50}$) of SARS-CoV-2. Histopathology

557   (HE) and immunohistochemistry (IHC) was used to assess pathology with the presence of

558   SARS-CoV-2 antigen in pulmonary sections at 3, 5 and 10dpi. (A-C), 3dpi. (A) Histopathology

559   is largely limited to bronchioles and terminal airway spaces and is not readily apparent at a low

560   magnification (H&E, 20x, size bar is 200um). (B) Immunohistochemical reaction highlights

561   antigen distribution in bronchioles and terminal airway spaces (20x, size bar is 200um). (C)

562   Bronchiolar epithelial cell immunoreactivity with limited antigen detection in alveolar spaces

563   (100x, size bar is 50um). (D-F), 5dpi. (D) Extension of cellular exudate from bronchioles into

564   alveolar spaces (H&E, 20x, size bar is 200um). (E) Immunoreactivity is detected along the

565   periphery of regions of pathology and has largely been cleared from bronchiolar epithelium (20x,

566   size bar is 200um). (F) Immunoreactivity is noted in type I and type II pneumocytes and few

567   alveolar macrophages (200x, size bar is 20um). (G-I), 10dpi (G) Resolving inflammation is

568   limited to bronchioles and adjacent terminal airways (H&E, 20x, size bar is 200um). (H) SARS-

569   CoV-2 immunoreactivity is not observed in regions of resolving inflammation (20x, size bar is

570   200um). (I) No immunoreactivity is observed (200x, size bar is 20um).

571   **Figure 6: Neither age nor sex affects shedding or disease following infection with SARS-**

572   **CoV-2.** To compare the effects of aging and sex on disease following SARS-CoV-2 infection,

573   young female and male (4-6weeks) and aged female and male (>6months) Syrian hamsters were

574   infected intranasally with 500 ID_{50} (10^3 $TCID_{50}$) of SARS-CoV-2. Samples were collected at the

575   time points noted. Weights were collected daily, shedding and viral loads in the lungs were

576   measured. (A) Daily weights. (B) Viral genome load recovered from oral swabs at each time

577   point. (C) Viral genome load recovered from rectal swabs at each time point. (D) Viral genome

578   load recovered from lungs at each terminal point. (E) Infectious titers in the lungs. ANOVA was

579   used to compare groups at each time where samples were collected. No significant differences

580   were observed between groups at any time point collected in in this study. *Note:* blue circles,

581   aged females; red circle, aged male; green circle, young female; purple circle, young male.

582   **Figure 7: SARS-CoV-2 infection of Interleukin-2 receptor subunit gamma knockout**

583   **hamsters (*IL2RG$^{-/-}$*) results in persistent infection and pneumonia.** *IL2RG* KO hamsters

584   lacking mature B-cells, T-cells and NK cells, were infected with 5×10^4 ID$_{50}$ (10^5 TCID$_{50}$) and

585   followed for 24 days to determine if disease developed. Weights were collected daily and

586   shedding from mucosal membranes and viral infectivity in the lungs were measured at the time

587   points noted. (A) Daily weights. (B) Viral genome load recovered from oral and rectal swabs at

588   each time point. (C) Infectious titers in the lungs. (D) Alveoli frequently contain macrophages,

589   neutrophils and sloughed epithelial cells, and are lined by numerous hyperplastic type II

590   pneumocytes (H&E, 200x). (E) Immunoreactivity is observed in hyperplastic type II

591   pneumocytes and macrophages (Anti-SARS-CoV-2 nuclear protein, 200x). *Note* (B): blue

592   circles, oral swabs; red circle, rectal swabs. Size bar is 100um.

593

594   **Supplemental Figure 1**: **Viral genomic RNA from various tissues.** Syrian hamsters were

595   infected intranasally with either 500 ID$_{50}$ (10^3 TCID$_{50}$) or 5×104 ID$_{50}$ (10^5 TCID$_{50}$) of SARS-

596   CoV-2. Tissue samples were collected at the time points noted. Numbers above each tissue

597   represent the number of tissues that infectious virus was isolated from. (A) Viral genome load

598   recovered from tissues at each time point following infection with 500 ID$_{50}$ SARS-CoV-2. (B)

599   Viral genome load recovered from tissues at each time point following infection with 5×10^4 ID$_{50}$

600   SARS-CoV-2. Statistical analysis using multiple T-tests found no significant differences

601   between either group at any time point samples were collected. *Note:* blue circle, 3dpi: red circle,

602   5dpi; green circle, 10dpi.

603   **Supplemental Figure 2**: **Gross pathology and lung weights.** To compare the effects of aging

604   and sex on disease following SARS-CoV-2 infection, young female and male (4-6 weeks) and

605   aged female and male (>6months) Syrian hamsters were infected intranasally with 500 ID_{50} (10^3

606    $TCID_{50}$) of SARS-CoV-2. Samples were collected at the time points noted. (A) Representative

607   gross pathology at indicated dpi. (B) Lung weights as percentage of body weights were recorded

608   at each time point as a measure for pneumonia. ANOVA tests were used to compare groups at

609   each time where samples were collected. Significant differences were not found between groups

610   sampled on the same day. Significant differences in lung weights were found in the groups

611   sampled at 5dpi vs those at 3dpi or 11dpi. *Note:* blue circles, aged females; red circle, aged

612   male; green circle, young female; purple circle, young male; orange circle, naive.

613
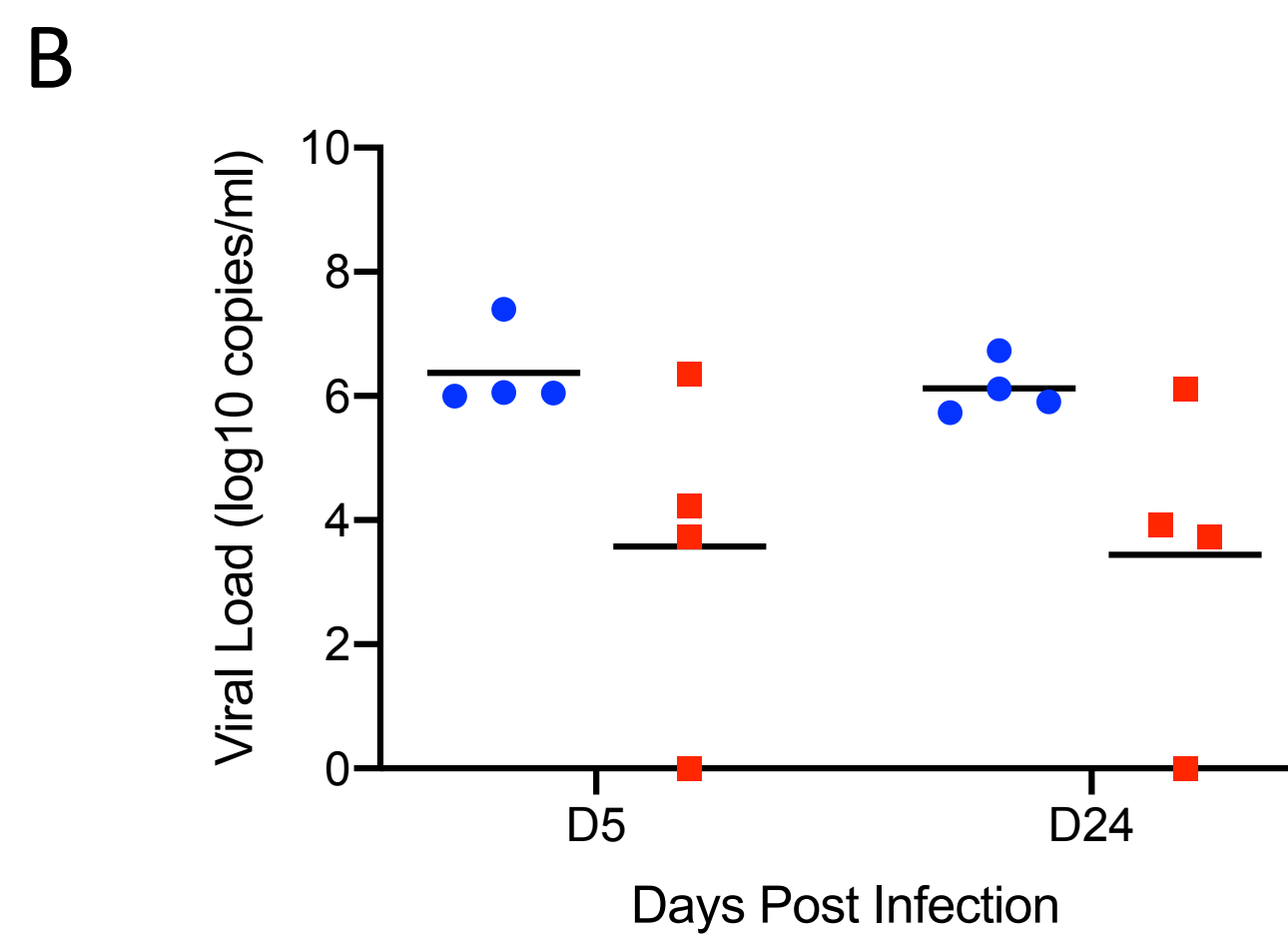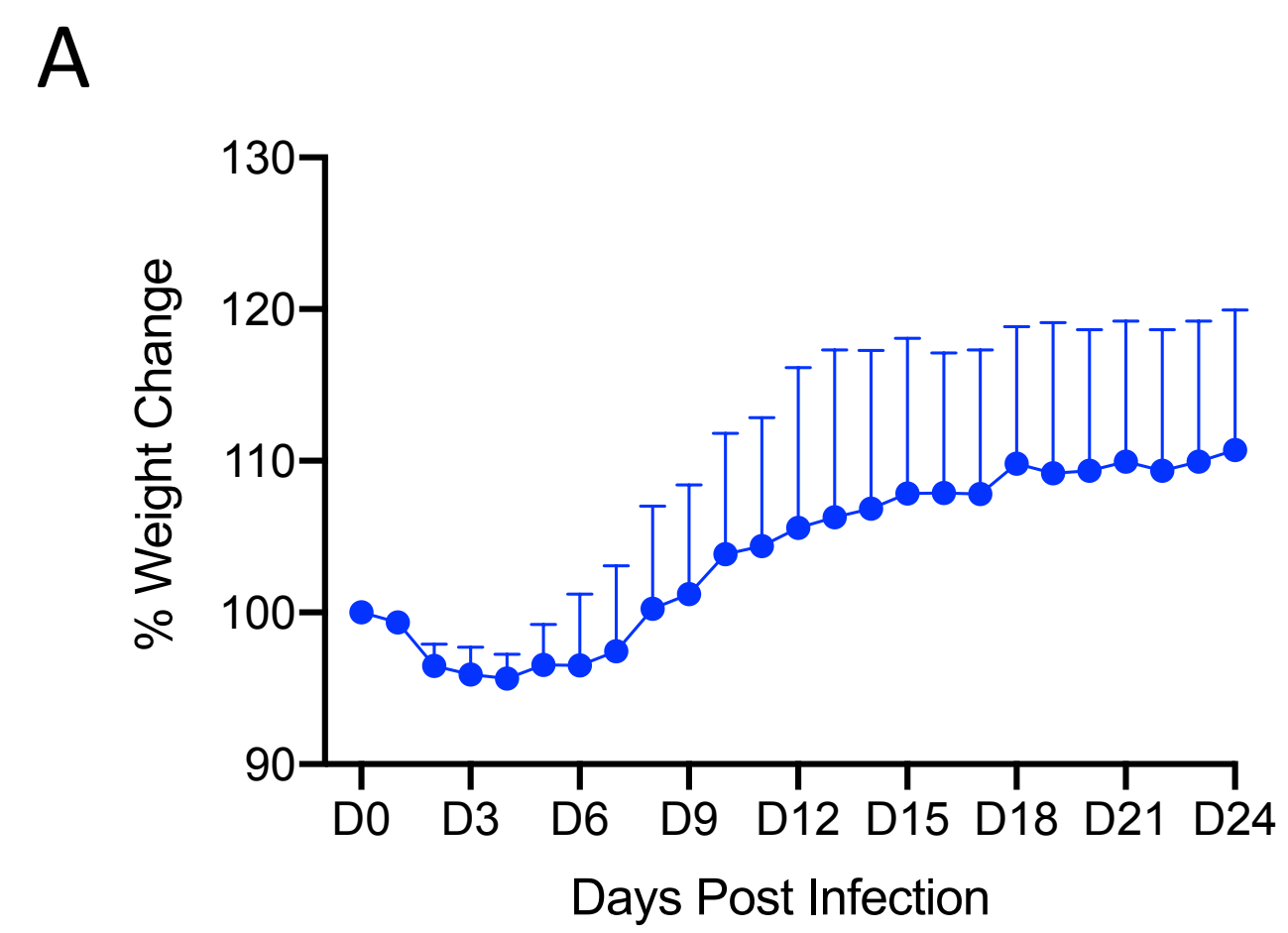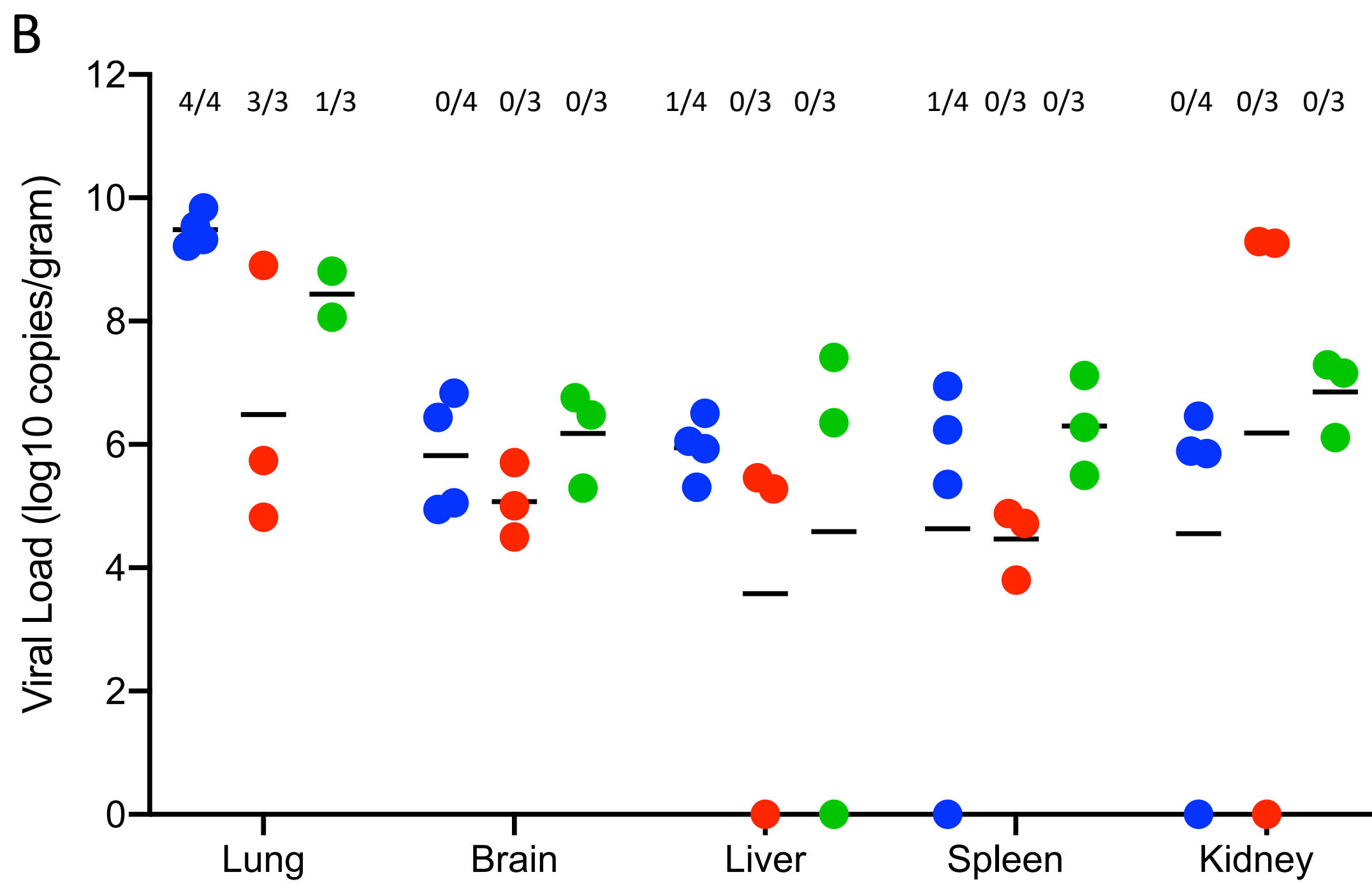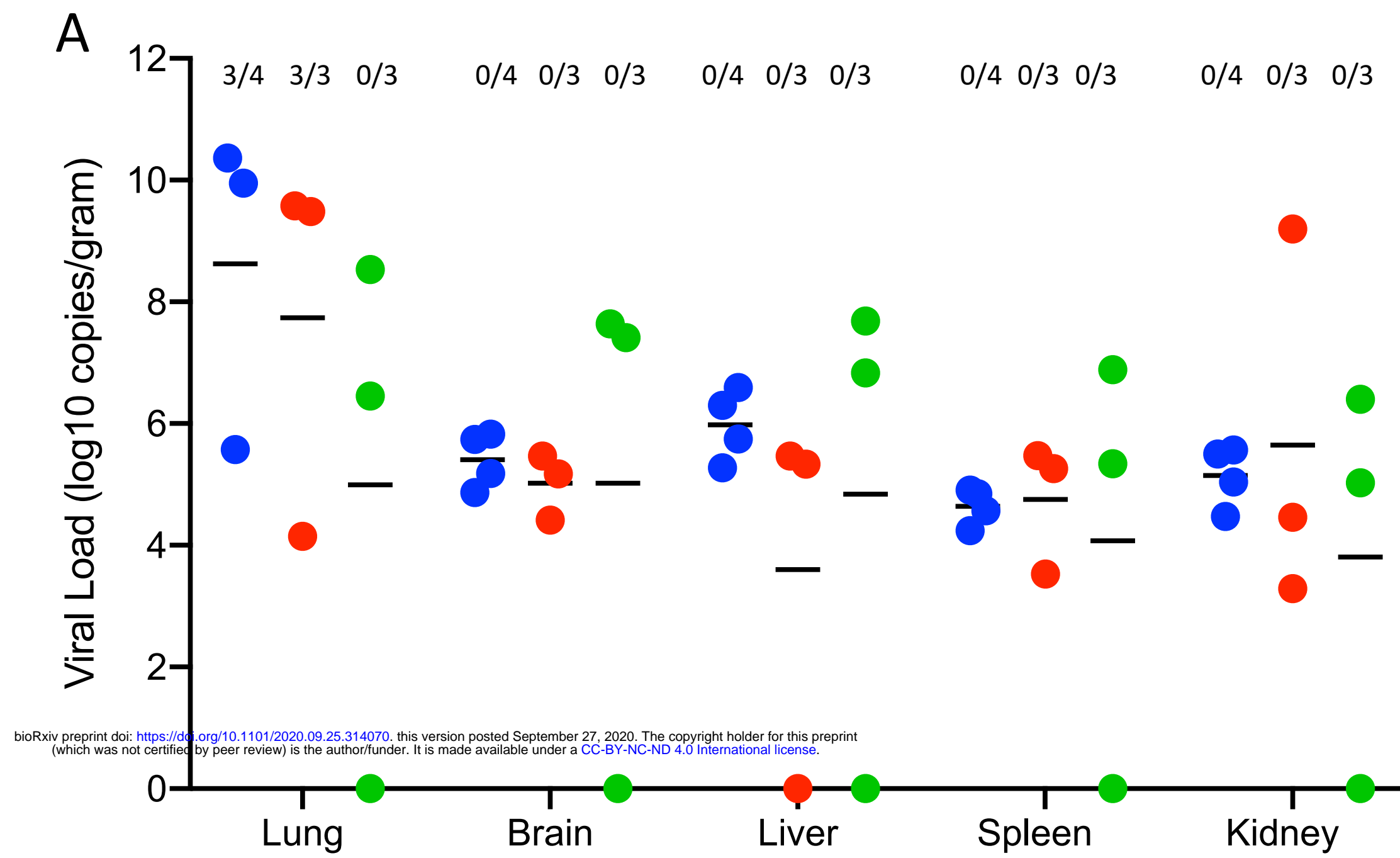
Figure 1

Figure 2

Figure 3

A
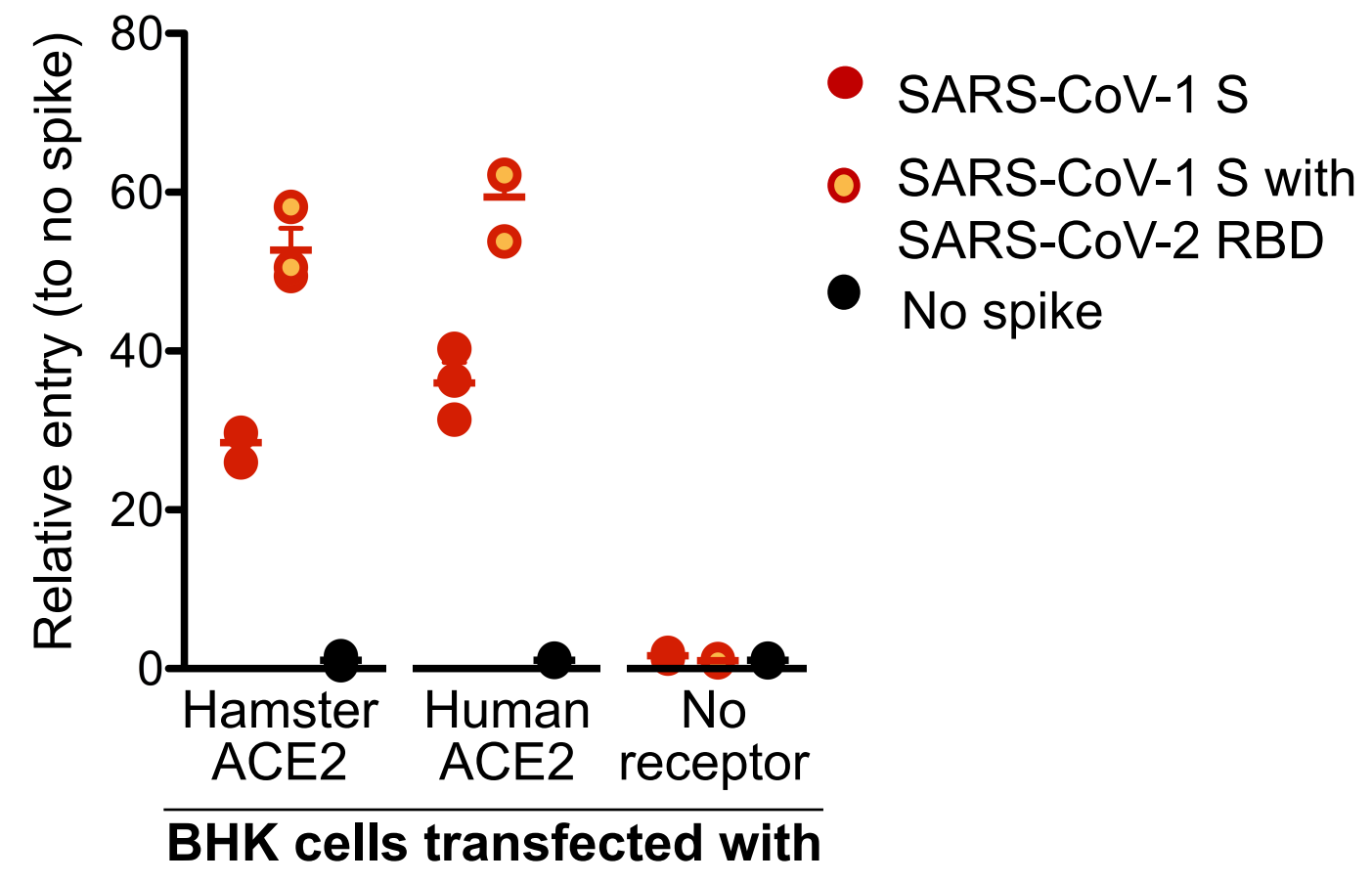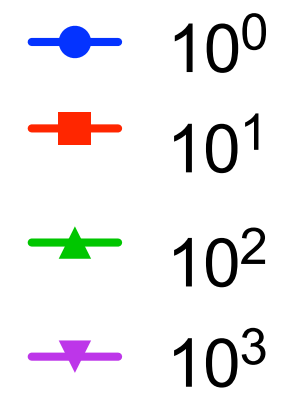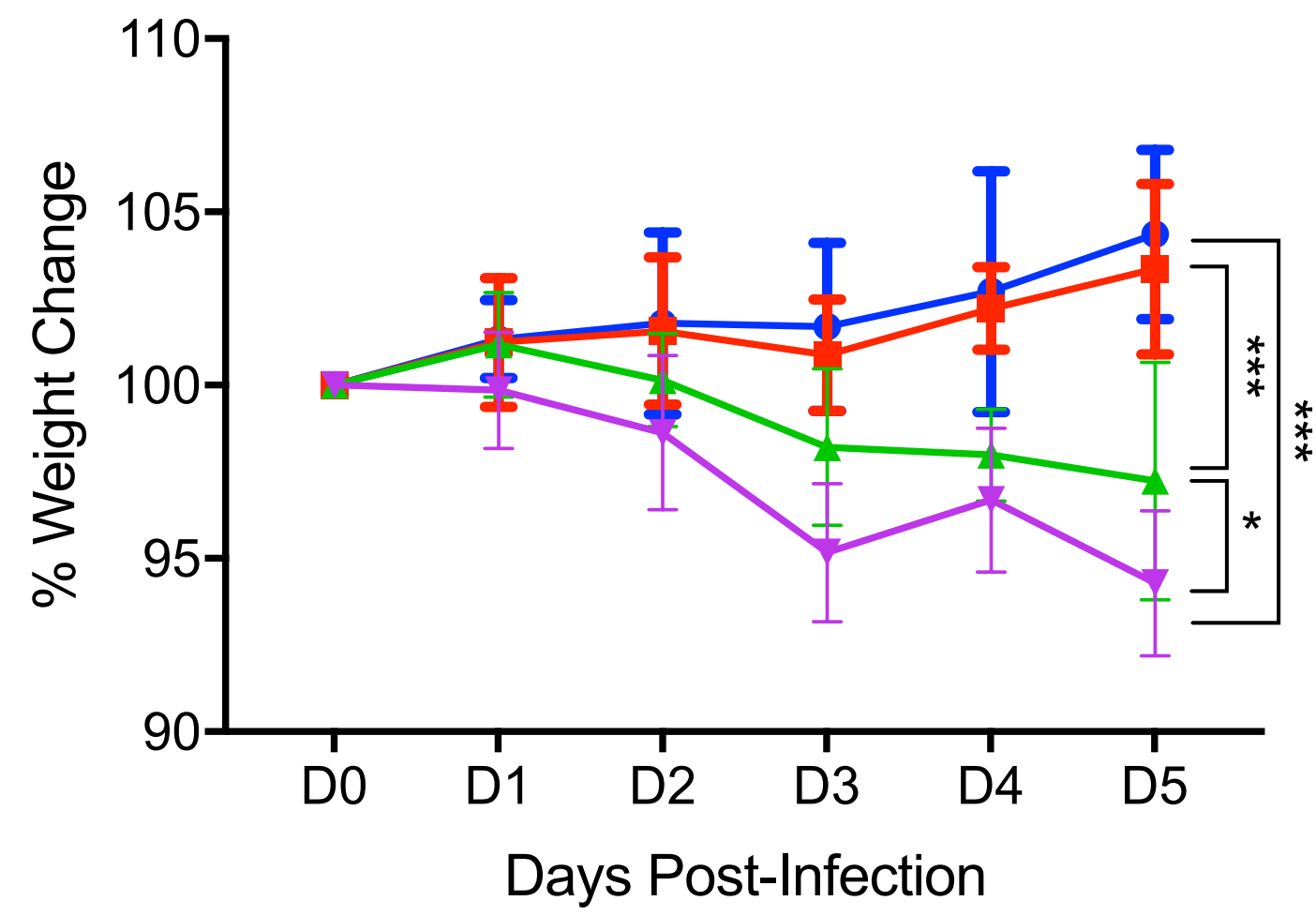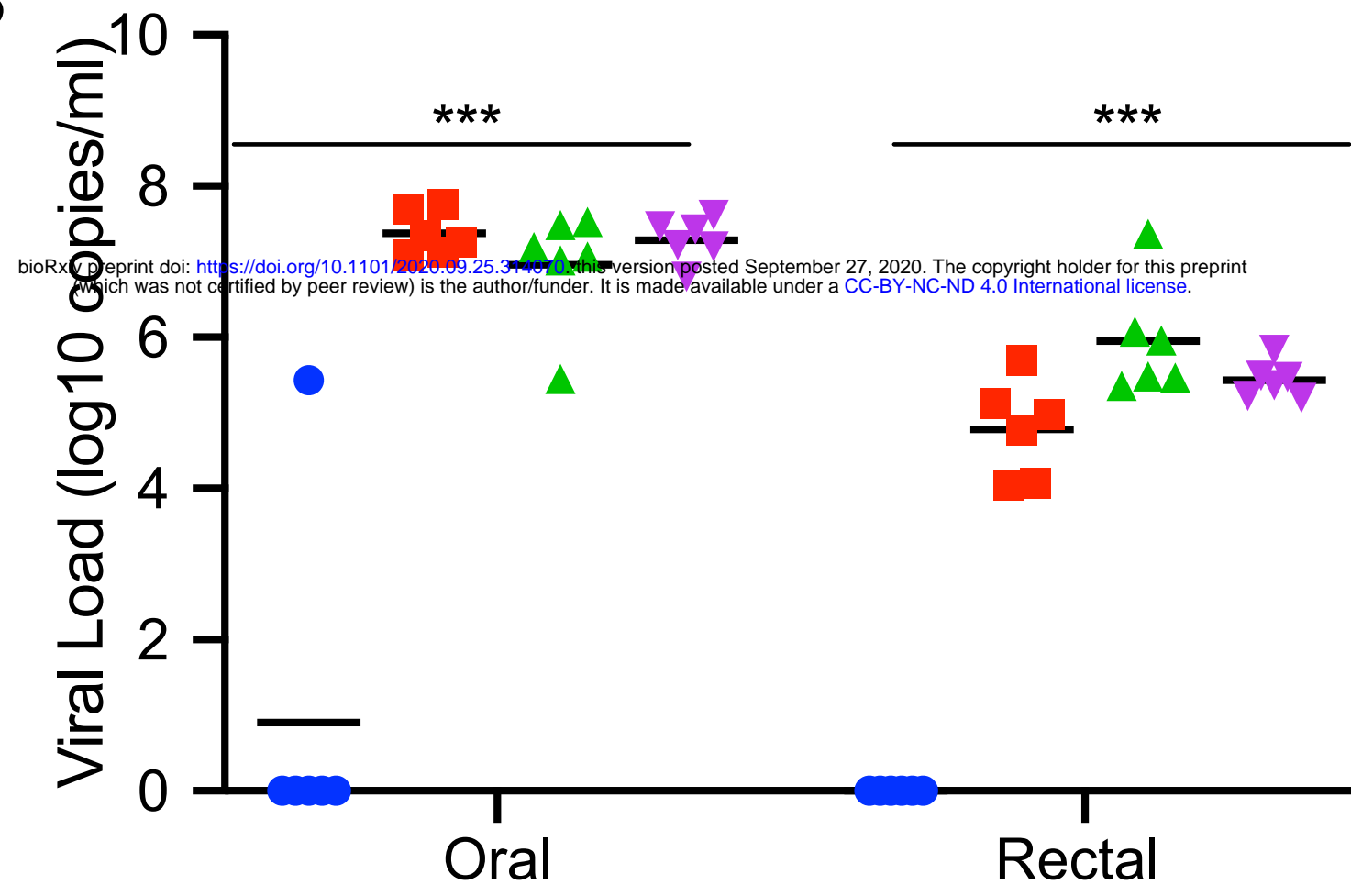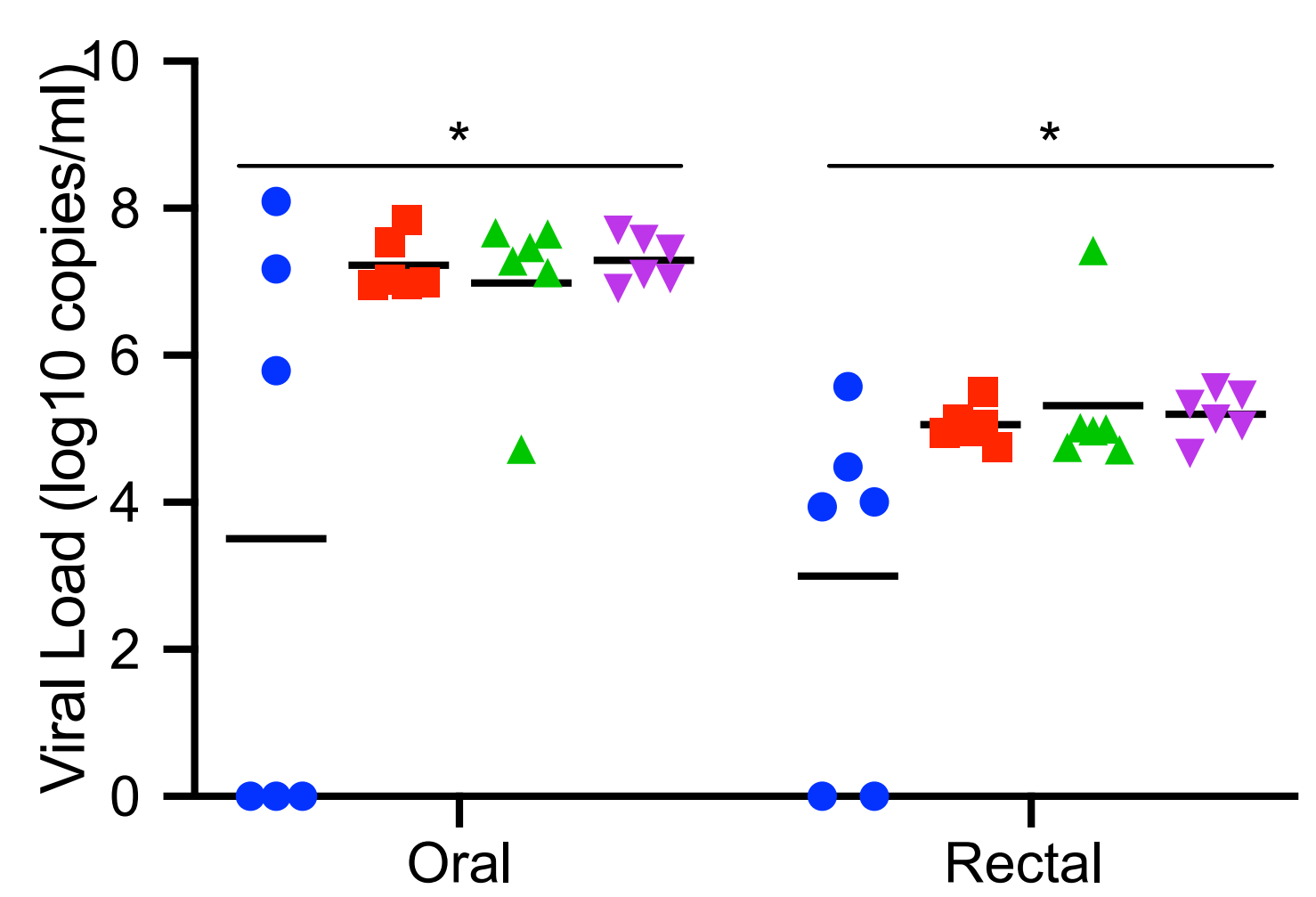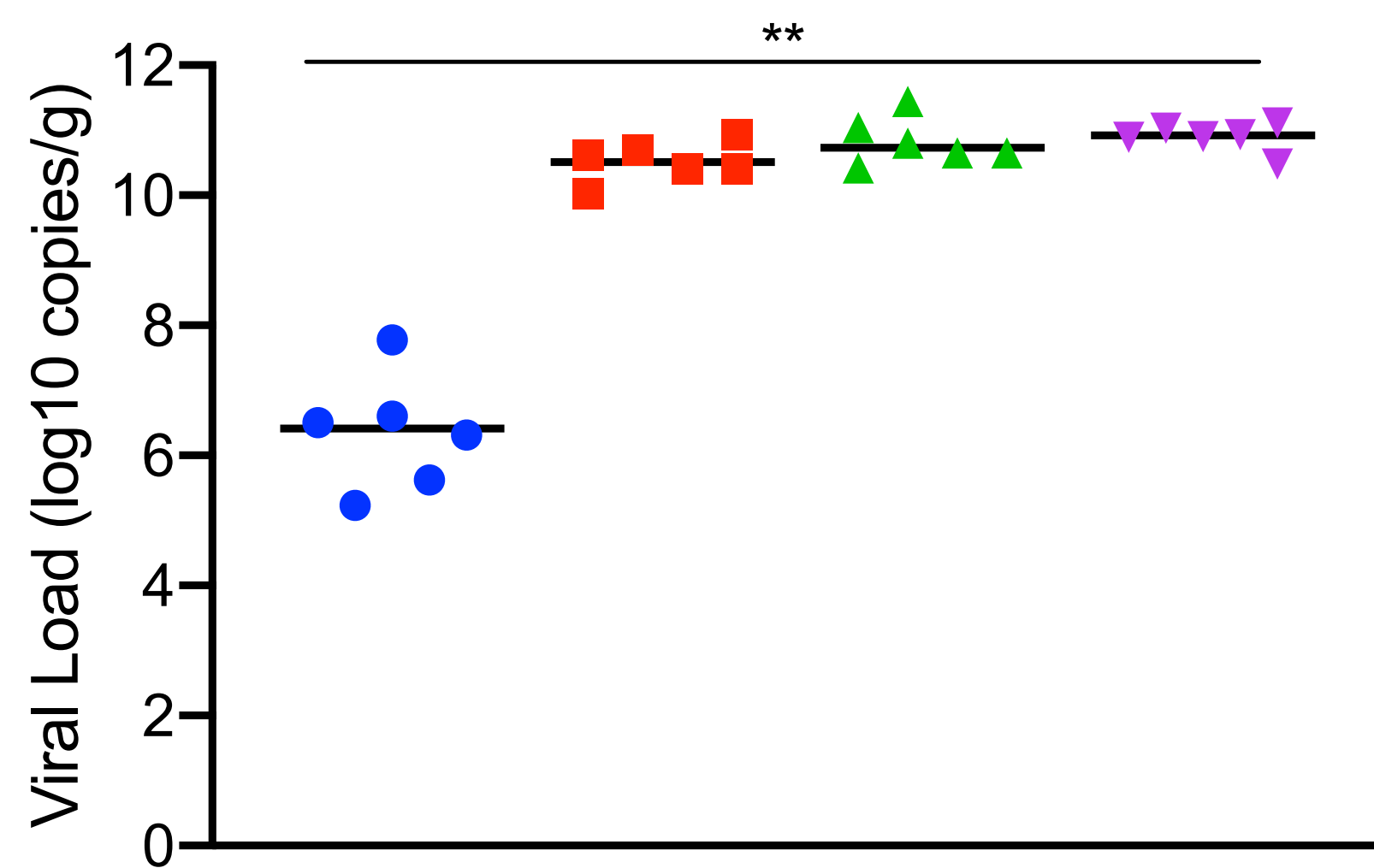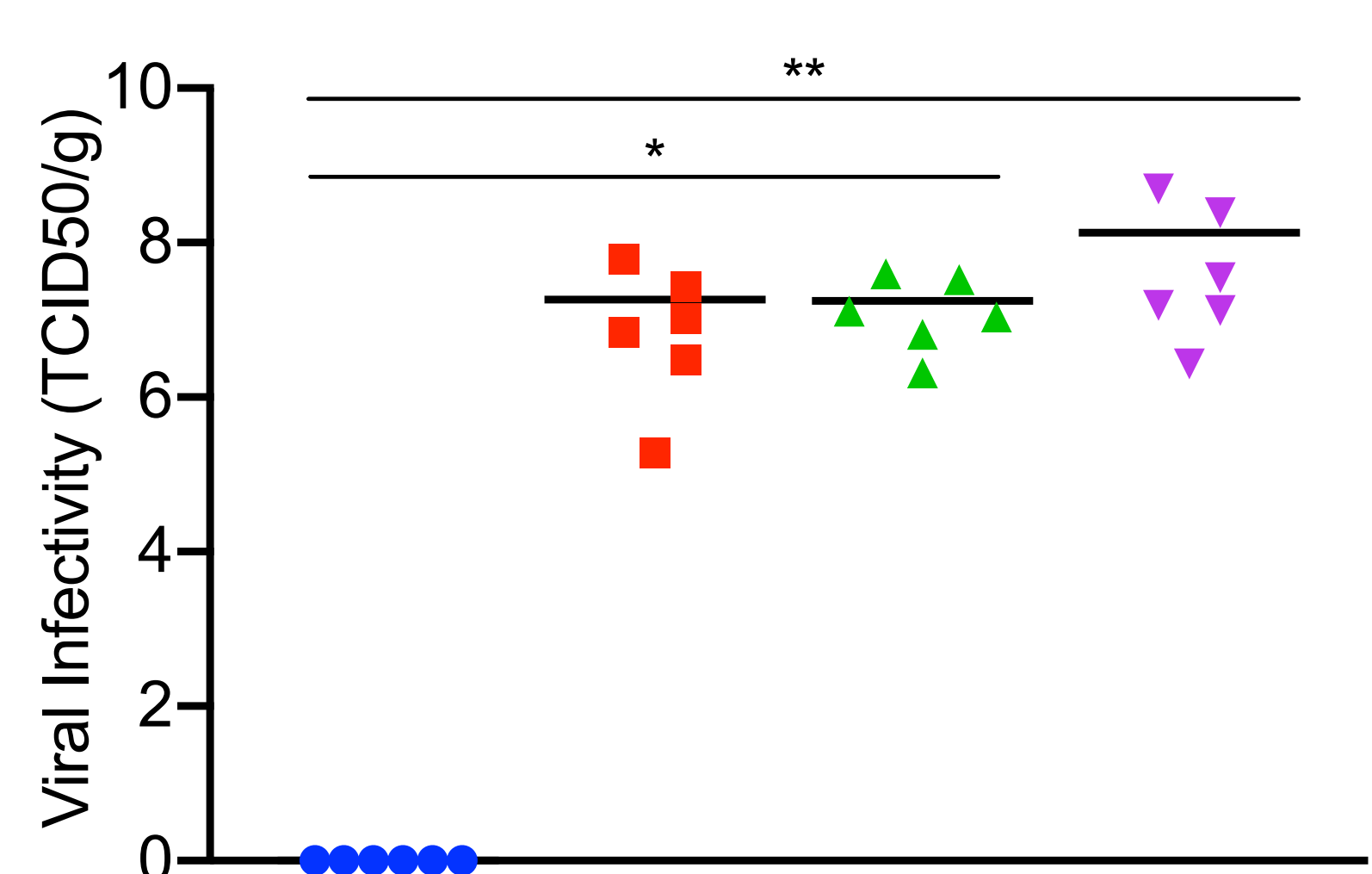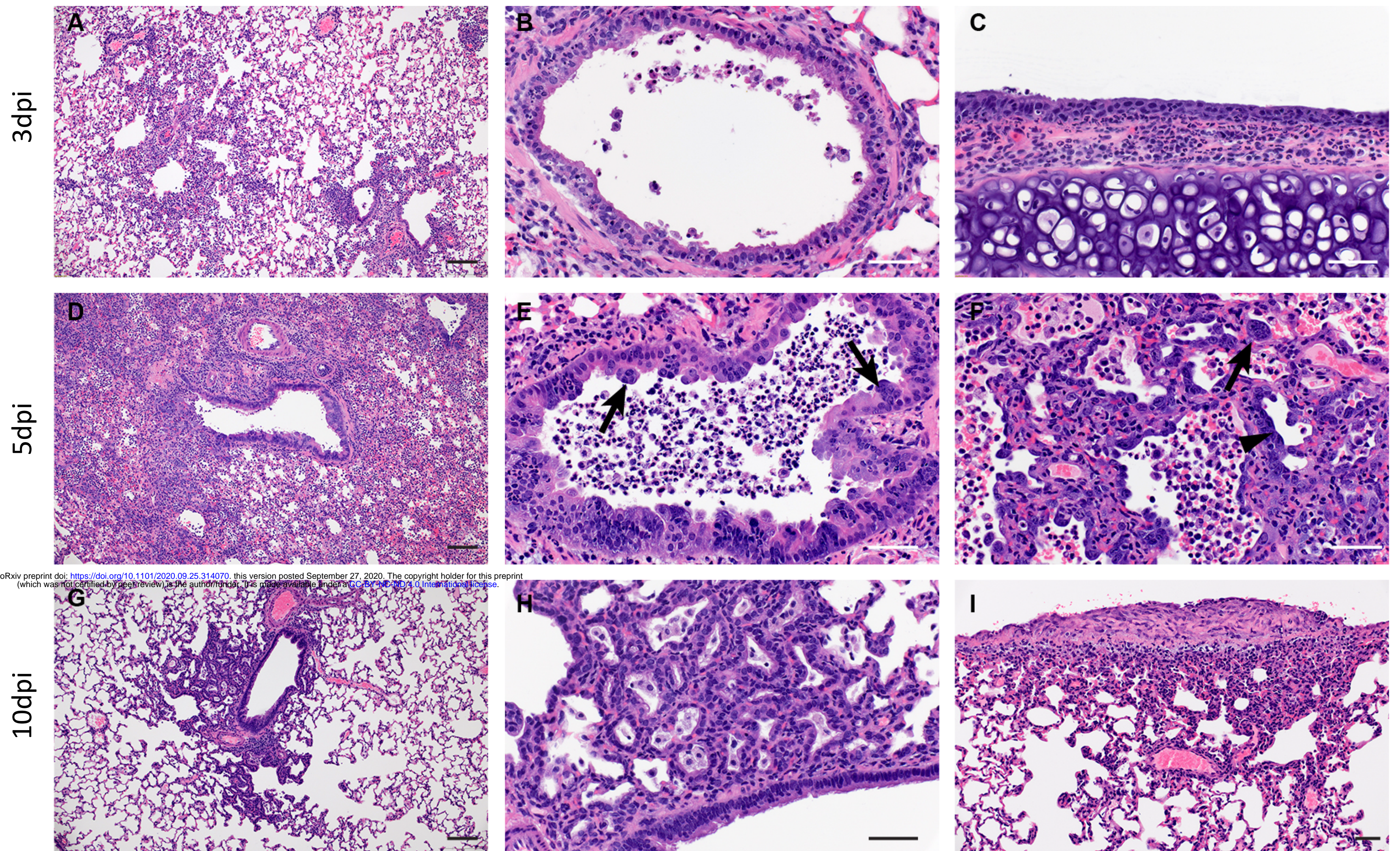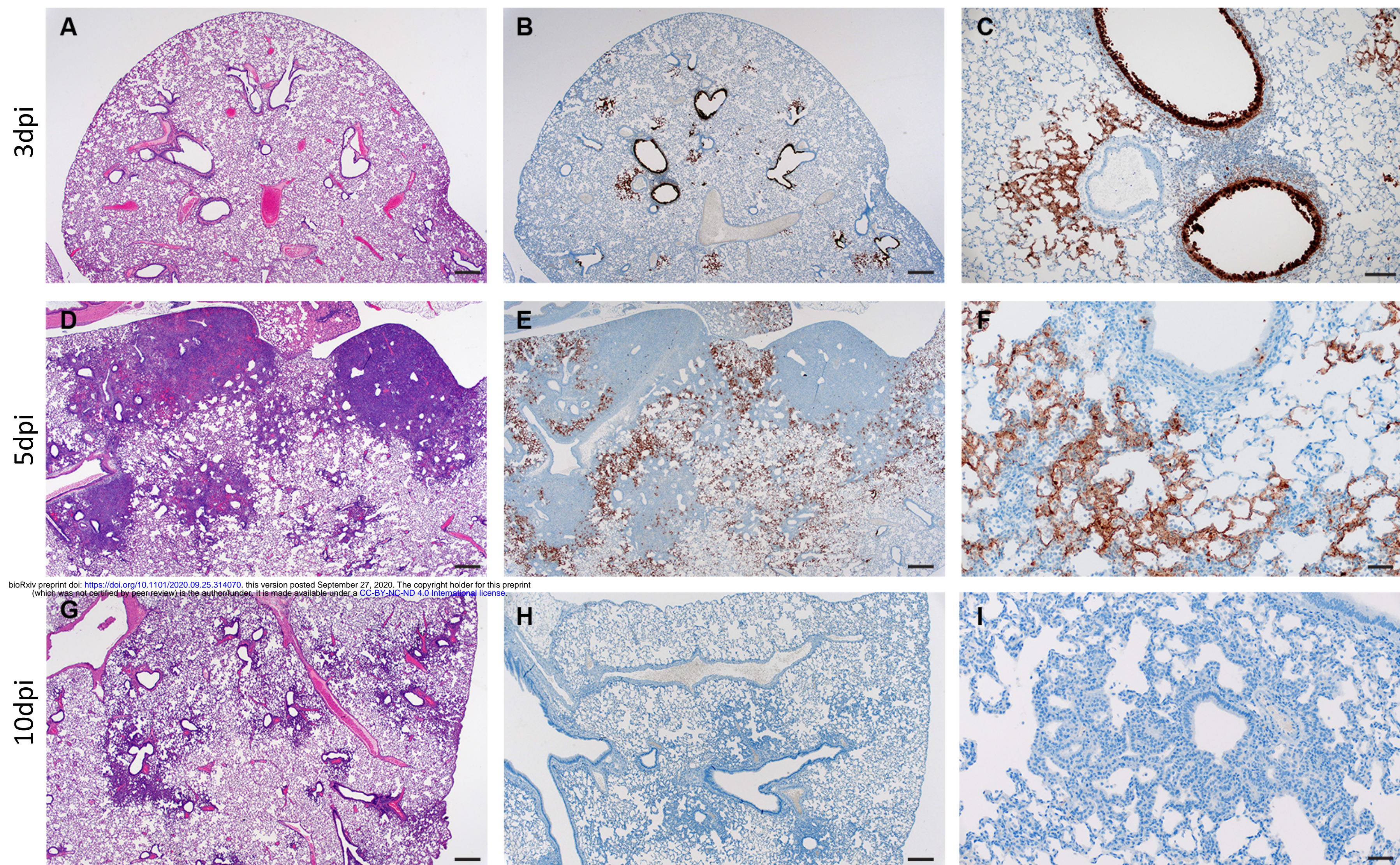
Figure 4

Figure 5

Figure 6
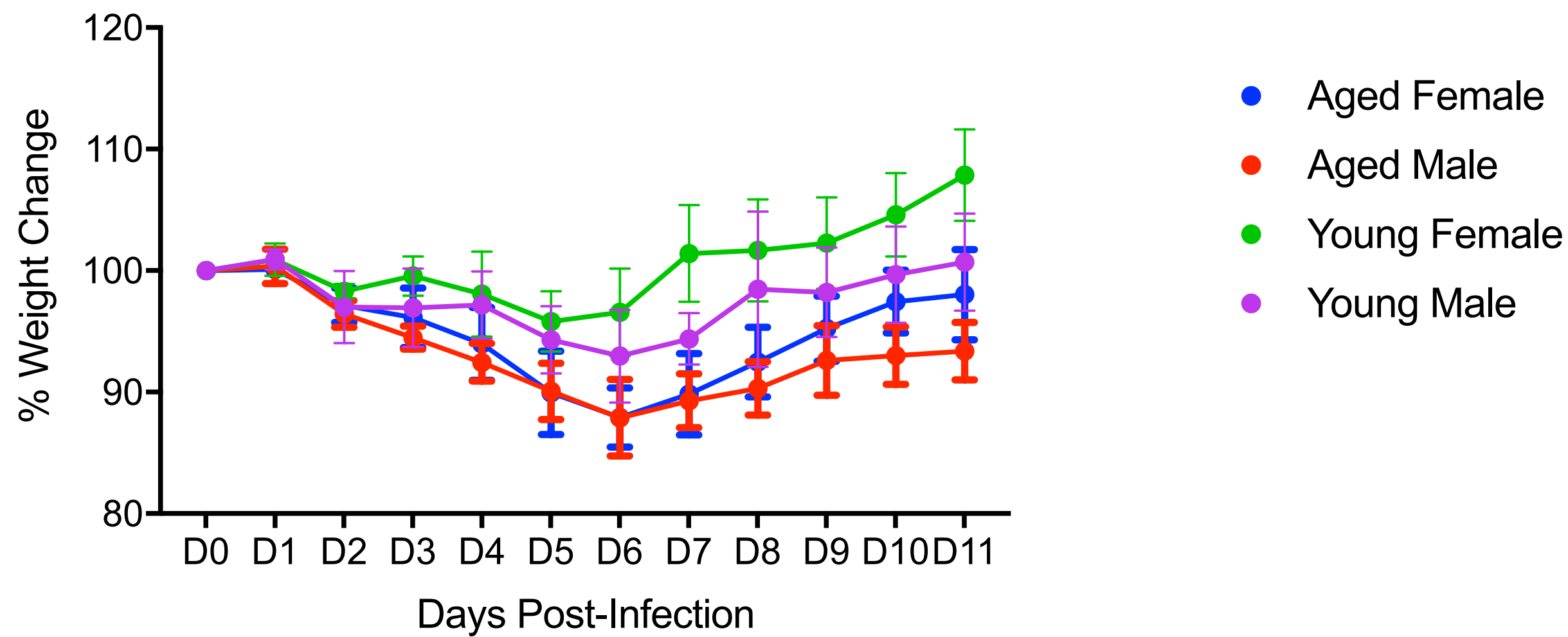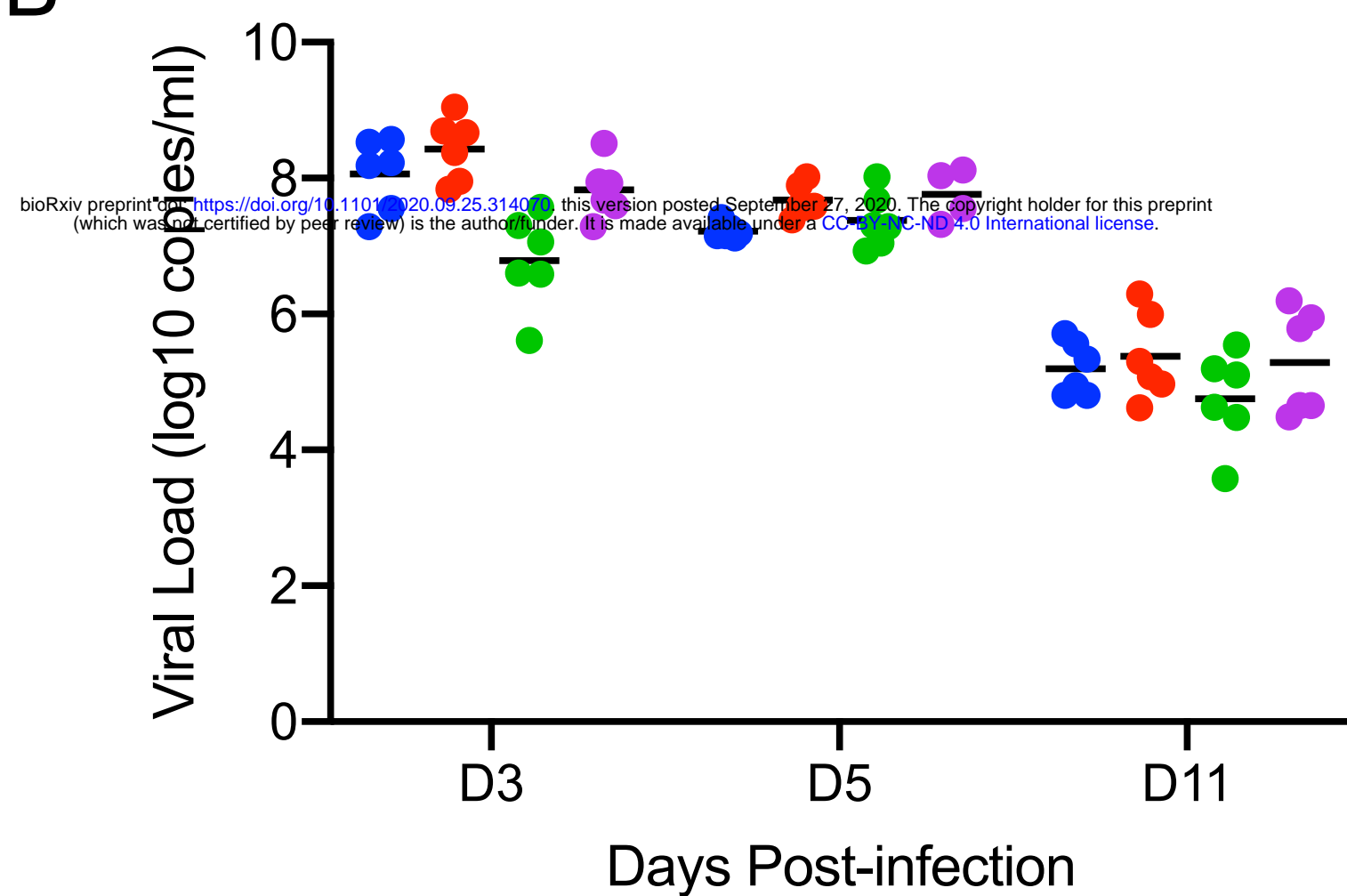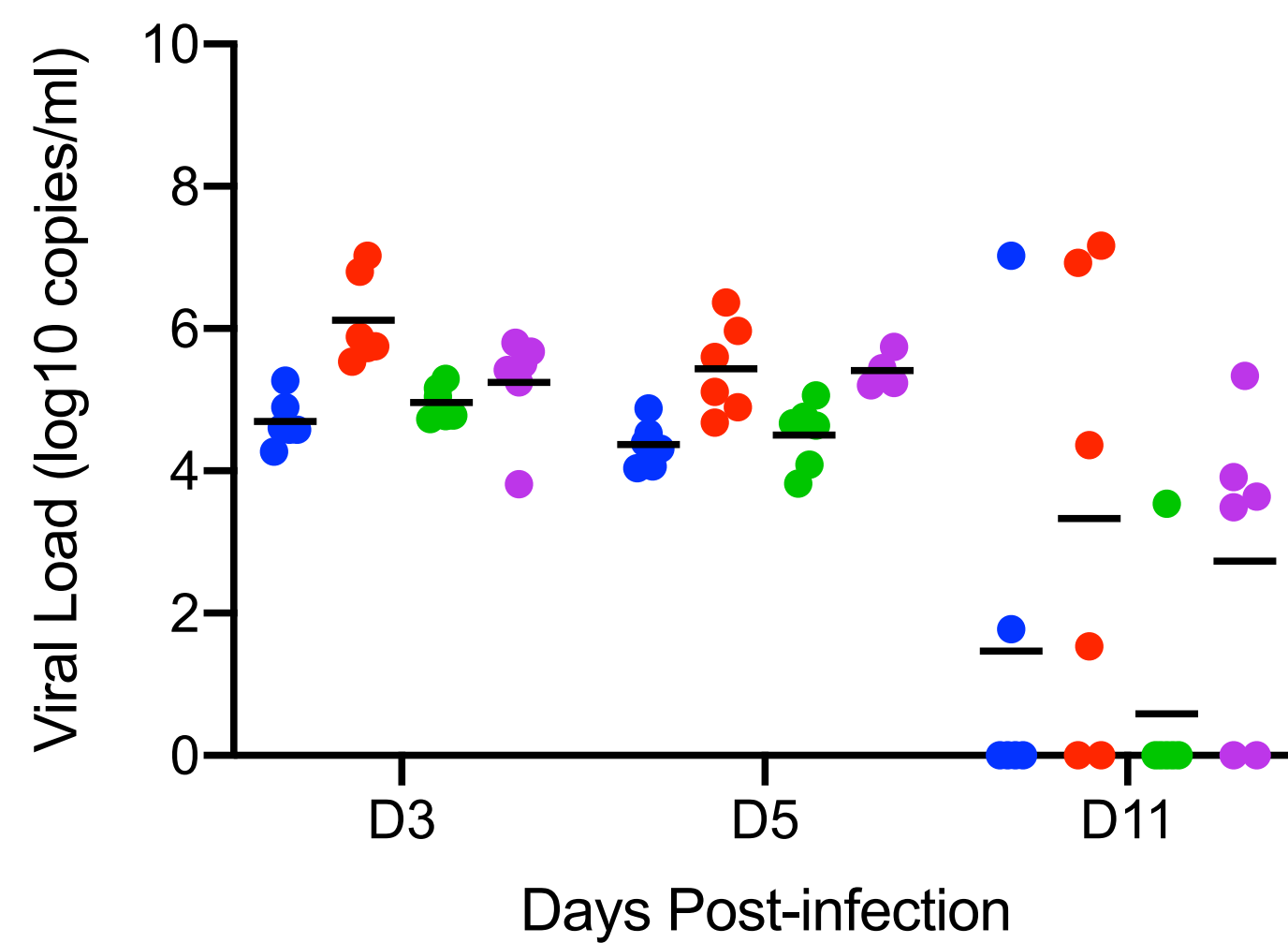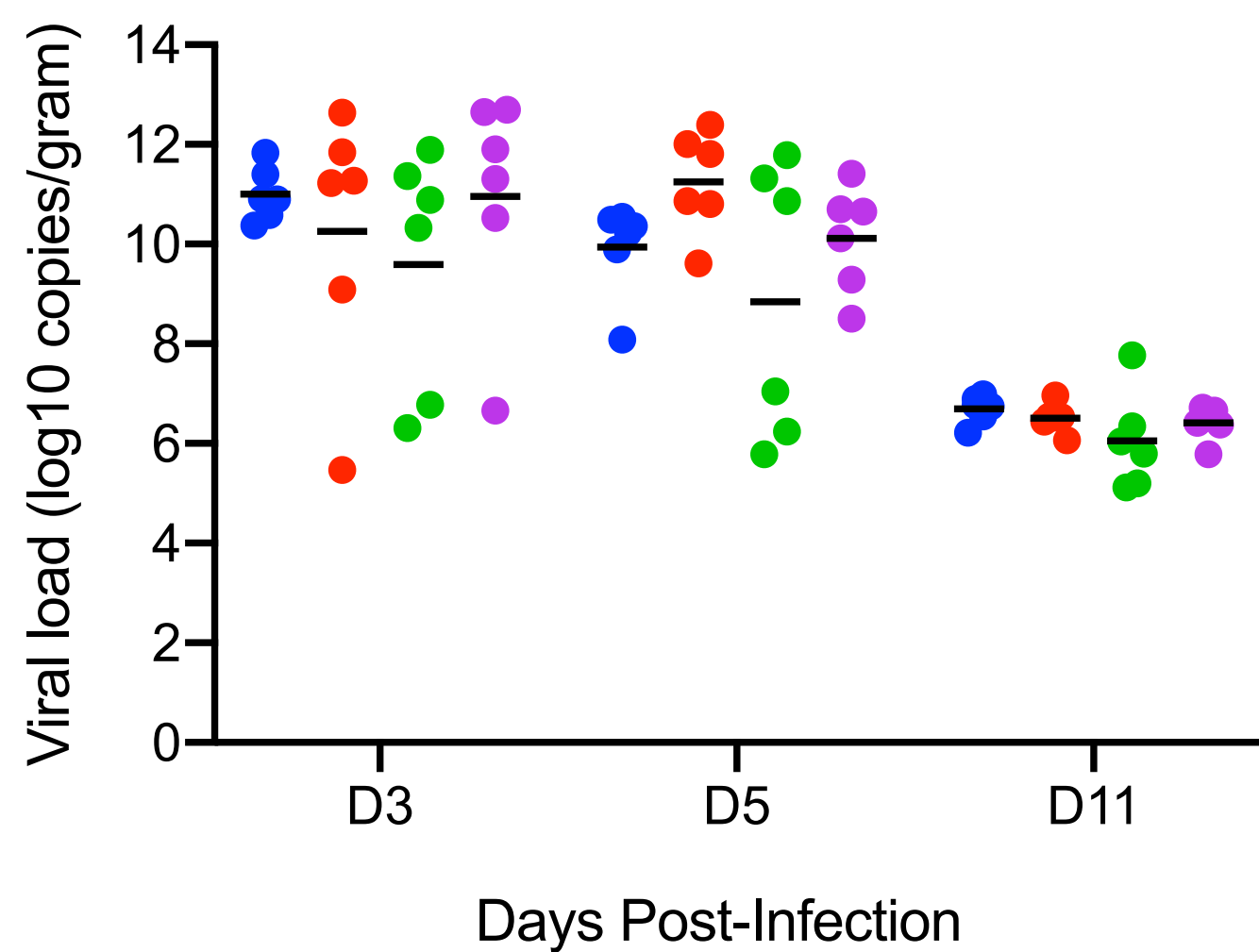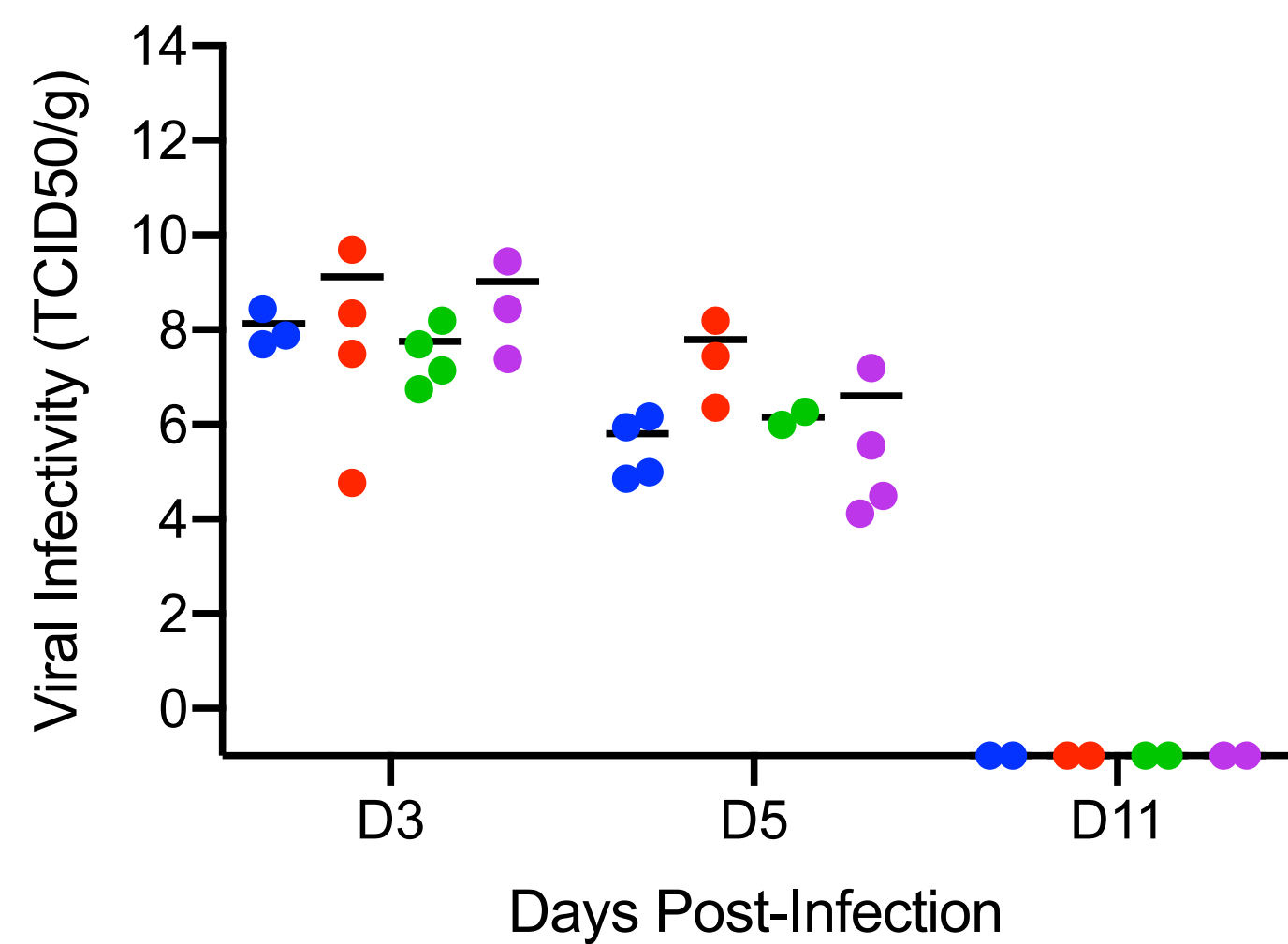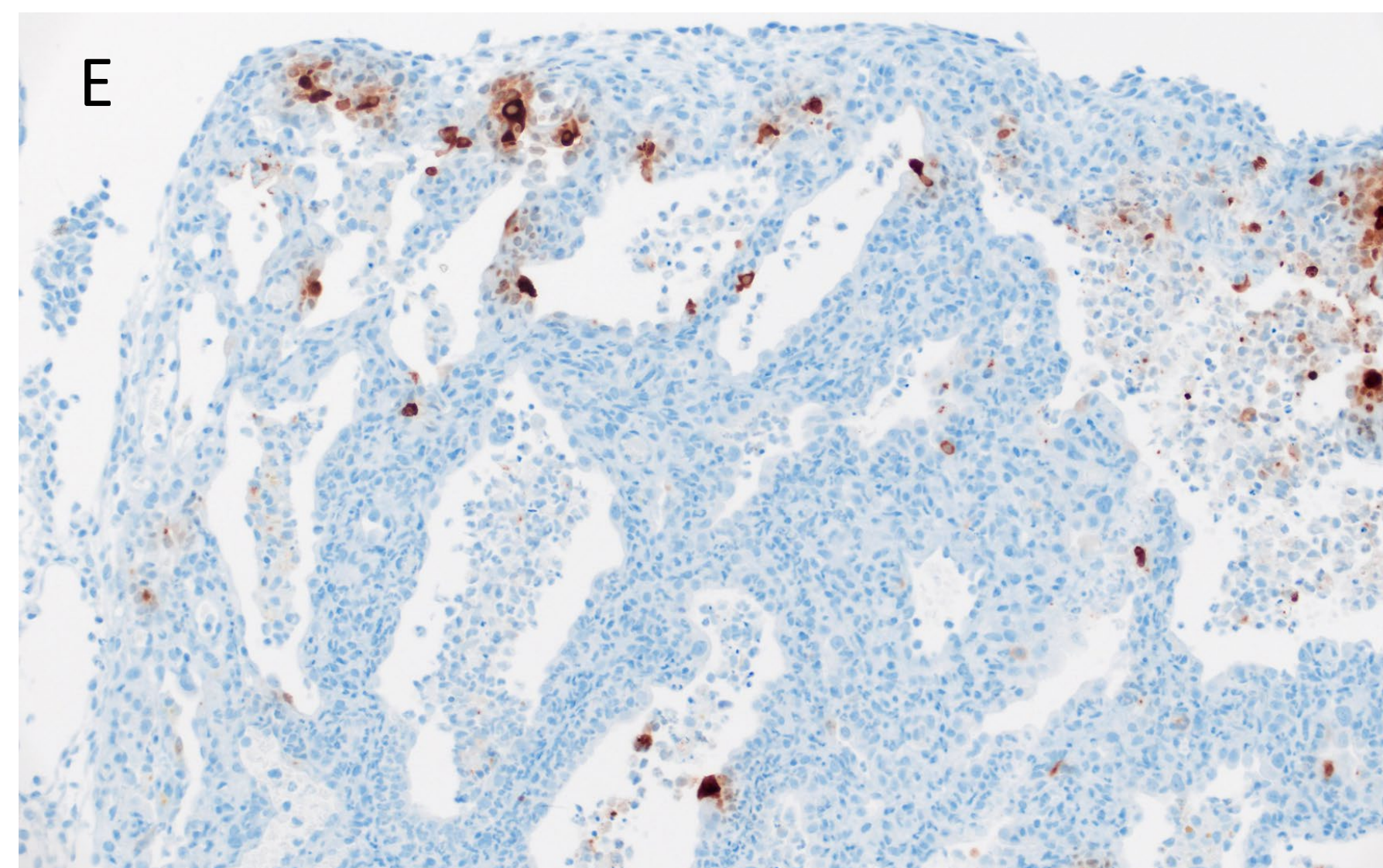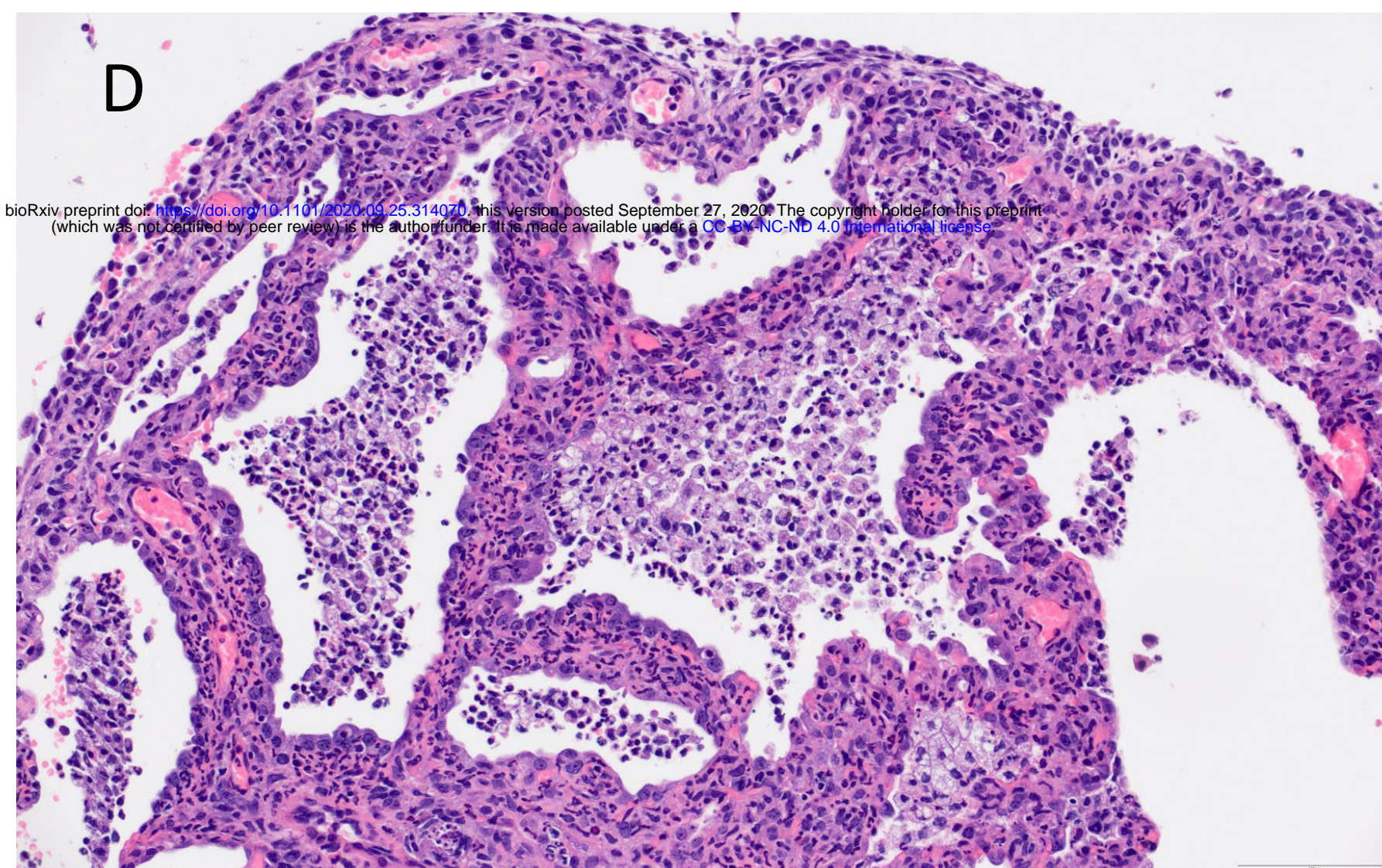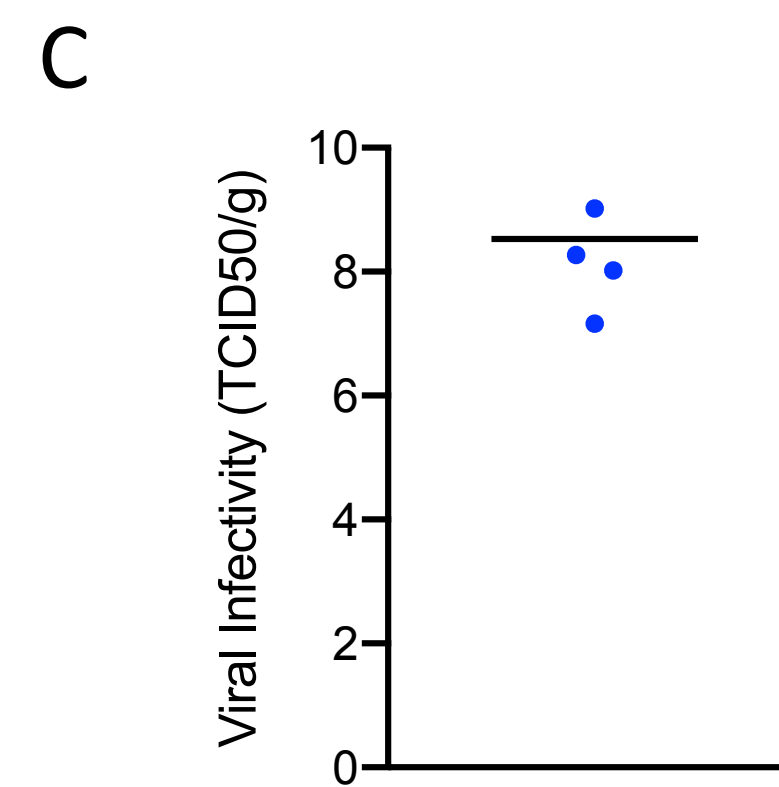
Figure 7

Supplemental Figure 1

Supplementary Figure 2

A

3 dpi   5 dpi   11 dpi

B